University of Limerick

Microchannel Pressure Flow & Heat Transfer Measurements

2007

Author

Niall O'Keeffe

0516538

Final Year Project

Submitted for the degree of

Bachelor of Engineering in Mechanical Engineering

Supervisors

Dr. Reena Cole

&

Dr. Cormac Eason

Declaration

The substance of the final year report is the original work of the author and due reference and acknowledgement have been made, where necessary, to the work of others.

Niall O'Keeffe

_____

(Student)

13th April 2007

Dr. Reena Cole

_____

(Supervisor)

13th April 2007

Dr. Cormac Eason

_____

(Supervisor)

13th April 2007

Abstract

The aim of the report was to investigate the Pressure Flow and Heat Transfer characteristics of rectangular and trapezoidal microchannels manufactured in silicon under a laminar regime. Each test sample consisted of 22 channels with nominal hydraulic diameters of 307.49μm and 317.78μm for the Deep Reactive Ion Etched channels (rectangular) and Wet Etched channels (trapezoidal) respectively.

Two experiments were performed according to the recommendation of previous work (Eason, 2005), to develop theoretical and experimental results for the pressure flow and heat transfer of the system. The mass flow rate and the pressure drop across the channels were measured along with the temperatures of the channel surface, the manifold surface and the fluid (deionised water) at the inlet and outlets for each microchannel test sample. Each data point was the assigned fluid properties according to the corresponding mean fluid temperature and collapsed to a single temperature curve by applying temperature compensation.

The results for the pressure drop and *fRe* values were considerably lower than the theoretical values for fully developed and simultaneously thermally and hydrodynamically developing flow. The DRIE experimental results showed no significant deviation from theory and the Wet Etch results were consistently lower than the theoretical correlations.

For the heat transfer experiments the manifold heating effect created large discrepancies in the experimental results however once this effect was taken into account, most of the heat transfer data converged onto a single curve. The resultant experimental Nusselt numbers showed a strong linear dependence on the Reynolds number and the data did not compare well with any of the theoretical correlations.

It was concluded that possible errors were obtained from the experimental system or the methods used to acquire the experimental data. It was also suggested that the channel area measurement using an optical microscope was not accurate enough for experiments of this nature and a Scanning Electron Microscope should be used.

Acknowledgements

This project has been ongoing for the last year and so there is plenty of people to acknowledge. I would mainly like to thank my supervisors *Dr. Reena Cole* and *Dr. Cormac Eason* for all their help throughout this final year. I would especially like to thank Cormac Eason for his continuous assistance and guidance on the subject matter of microchannels.

I must also acknowledge the assistance of :

Ryan Enright, for his assistance with the LabVIEW and supplying the thermocouple amplifier,

Paddy O'Regan, for his general assistance inside the Laboratory in the Stokes Research Institute

I am also grateful to everyone at the Stokes Research Institute & the Department of Aeronautical & Mechanical Engineering in the University of Limerick for any help throughout the year.

Special thanks must also go to Barbara Keogh, my family, and friends, for all the help and support throughout my time in the University of Limerick.

Nomenclature

Symbol	Description	Unit
A	Channel cross sectional area (CSA)	m^2
A_{Comp}	Exact CSA of channel measured from a CAD model	m^2
A_M	Manifold CSA/Number of channels (n)	m^2
A_t	Total convecting surface area of the channels	m^2
A_{Theory}	CSA of channel measured from direct width/height data	m^2
A_{tot}	Total channel area in a single sample ($A_{tot} = nA$)	m^2
A_1	Initial cross sectional area of a channel	m^2
A_2	Final cross sectional area of a channel	m^2
$B_{1,2}$	Muzychka and Yovanovich Constants	No Unit
C_{1-4}	Muzychka and Yovanovich Constants	No Unit
D_h	Hydraulic diameter (*4A/Wetter Perimeter*)	m
H	Channel height	m
I	Electrical Current	A
K_c	Loss coefficient due to a sudden contraction	No Unit
K_e	Loss coefficient due to a sudden expansion	No Unit
K_L	Loss coefficient due to area change in a channel	No Unit
L	Channel Length	m
L'	Distance along channel used for calculating x^+	m
M	Blending parameter $\{M = 2.27 + 1.65Pr^{1/3}\}$	No Unit
Nu	Average Nusselt number = (hD_h/k)	No Unit
$Nuexp$	Experimentally measured Nusselt number	No Unit
Nu_{Muzy}	Nu (Muzychka and Yovanovich, 2004)	No Unit
$Nu_{Muzyavgq}$	Average of upper and lower limits calculated by changing γ for Nu_{Muzy}	No Unit
Nuq	Constant surface heat flux developed flow Nusselt number for 3 walls heated condition	No Unit
$Nu_{SeiderTate}$	Seider and Tate Correlation Nu correlation	No Unit
$NuTheory$	Theoretical Nusselt number based on most relevant correlation available for a particular channel	No Unit

P	Pressure	Pa
P_L	Pressure drop across a channel	Pa
PL	Theoretical Darcy pressure drop along channel length	Pa
$P_{L_{Comp}}$	Pressure drop after area compensation	Pa
P_{Li}	Inlet pressure drop due to flow area change	Pa
$PLMuzy$	Pressure drop found using friction factor	Pa
P_{Lo}	Outlet pressure drop due to flow area change	Pa
$P_{L_{Theory}}$	Pressure drop before area compensation	Pa
$PLtot$	Total theoretical pressure drop for channel including Manifold and entrance/exit losses and flow friction	Pa
Pr	Prandtl number $(\mu c_P / k)$	No Unit
$\dot{Q}$	Heat transfer rate	W
$\dot{q}$	Heat flux	W/m^2
Re	Reynolds number $(\rho u D_h / \mu)$	No Unit
$\mathrm{Re}_{\sqrt{A}}$	Reynolds number $(\rho u \sqrt{A} / \mu)$	No Unit
T	Temperature	°C
T_{avgF}	Average fluid temperature in system (T_{inF} + T_{outF})/2	°C
T_{avgS}	Average surface temperature in system (T_{inS} + T_{outS})/2	°C
T_{inF}	Temperature of fluid at inlet	°C
T_{inS}	Temperature of channel surface at inlet	°C
T_{outF}	Temperature of fluid at outlet	°C
T_{outS}	Temperature of channel surface at outlet	°C
V	Voltage measured by voltmeter	V
W	Channel width	m
W_b	Base width of trapezoidal channel	m
c_p	Specific heat capacity	J/kgK
d	Distance	m
f	Friction factor	No Unit
f_{app}	Apparent friction factor accounting for developing flow	No Unit
$f(Pr)$	Friction factor for variation in Pr ; Function of Prandtl No.	No Unit
g	Acceleration due to gravity (9.80665m/s^2)	m/s^2
h	Average convection heat transfer coefficient	W/m^{2}K

h_{fg}	Latent heat of vaporisation	J/kg
k	Thermal conductivity	W/mK
$\dot{m}$	Mass flow rate through the system	kg/s
$\dot{m}_{ch}$	Mass flow rate through a single channel	kg/s
n	Number of channels in a sample	No unit
u	Mean fluid velocity in a channel	m/s
x	Distance along fin between channels $0<x<H$, Any variable of interest or value measured on x-axis	-
$\bar{x}$	Average value of x, $\bar{x} = \sum_{i=1}^{n} \frac{x_i}{n}$	-
x^+	Dimensionless Channel Length, $x^+ = \frac{2L'}{D_h \,\mathrm{Re}\,\mathrm{Pr}}$	No Unit
z^+	Dimensionless Length $\mathrm{z}^+ = \mathrm{L} \big/ \left(\sqrt{A}\mathrm{Re}_{\sqrt{\mathrm{A}}}\right)$	No Unit
z*	Dimensionless Length $z^* = z^+ \big/ \mathrm{Pr}$	No Unit

Greek Symbols

β	Volume Expansion Coefficient	1/K
ε	Channel aspect ratio {W/H}	No Unit
γ	Variable from Muzychka (2004) equal to 0.1 or -0.3	No Unit
θ	Burette tilt angle relative to vertical	°
μ	Fluid viscosity	kg/m.s
π	Ratio between circumference and diameter of a circle π = 3.14159265358979	No Unit
ρ	Fluid density	kg/m^2
σ_x	Sample Standard Deviation of x, $\sigma_x = \sqrt{\frac{\sum_{i=1}^{n} (x_i - \bar{x})^2}{n-1}}$	Same Unit as x
ϕ	Wall angle	Degree

Subscripts

L	Liquid
T	Property at temperature T
V	Vapour
Comp	Area Compensated
_acomp	Calculated value normalised to a standard temperature (20°C)
exp	Experimentally measured value
F	Property of fluid
i	Inlet manifold/state
in	State at channel inlet
M	Property of Manifold
Muzy	Muzychka and Yovanovich correlation
o	Outlet manifold/state
out	State at channel outlet
q	Suffix to specify Nusselt value is for constant surface heat flux conditions
S	Property of microchannel surface
Theory	Value calculated theoretically
t	Suffix to Nusselt value is for constant surface temperature conditions
20	Property at 20°C

Abbreviations

CAD	Computer Aided Design
CCD	Charge Coupled Device or Colour Capture Device *(image sensors)*
CFD	Computer Fluid Dynamics
CD	Compact Disk
CI	Confidence Interval
CSA	Cross Sectional Area
DAQ	Data Acquisition
DI	Deionised (Usually refers to water)
DRIE	Deep Reactive Ion Etching
EDM	Electro-discharge Machining
FEP	Fluorinated Ethylene Propylene

HF	Hydrofluoric Acid
IC	Integrated Circuit
ID	Inside Diameter
ITRS	International Technology Roadmap for Semiconductors
KOH	Potassium Hydroxide
LabVIEW	Laboratory Virtual Instrumentation Engineering Workbench
LASER	Light Amplification by Stimulated Emission of Radiation
LPCVD	Low Pressure Chemical Vapour Deposition
MCM	Multchip Module
MEMS	Micro Electro-Mechanical Systems
OD	Outside Diameter
PC	Personal Computer
PCI	Peripheral Component Interconnect
PID	Proportional, Integral and Derivative *(method of control)*
PTFE	Polytetrafluoroethylene *(or Teflon)*
RPM	Revolutions Per Minute
SEM	Scanning Electron Microscope
SHC	Specific Heat Capacity
Si	Silicon
SI	Système Internationale (Metric Unit System)
Si_3N_4	Silicon Nitride
UV	Ultra Violet

Table of Contents

List of Figures

List of tables

1.0 Introduction

In recent times there has been an increasing demand for miniaturised electronic components and so more electronic components are crammed into smaller spaces, creating devices with extremely high power densities (Watts per cm^2). As a result of these high power densities, the limits of conventional forced convection air cooling are being rapidly approached. This phenomenon is most clearly evident in the development of computer microprocessors where the power dissipation, number of transistors and clock frequency have increased exponentially, placing huge stresses on the current cooling technology (Belhardja *et al.* 2003).

The rate of increase in microprocessor development was initially predicted by Gordon Moore in 1965 and later revised in 1975 to state that the number of transistors in processor chip would double every two years. The growth of transistor population in Intel's microprocessor chips has consistently matched this trend over the past thirty years (Mendelson, 1979). In Figure 1.1 the International Technology Roadmap for Semiconductors (ITRS) 2006 update predictions, for the advances in processor chip power are shown from the year 2004 until 2020 (ITRS, 2006).

Figure 1.1 Details the ITRS 2006 update predictions for the power advances in processor chips until 2020.

It can be seen that the overall chip power and power density in high performance processors (used in supercomputers and avionics) will rise until 2011 and 2016 respectively and for the cost performance chips (used in desktops and notebook PC's) the power density will be maintained at a constant level from 2008 by increasing the

processor size in proportion to the rise in chip power. These figures represent the current estimate of growth in this industry and are based on the consensus of experts from the semiconductor area (Eason, 2005). The ITRS also predicts over the same period that the maximum operating surface temperature of a processor chip will be within 90 - 100°C after which overheating will occur causing a reduction in performance and an increased risk of failure.

It is a well known fact that the reliability of electronic components is dependant on its temperature and therefore it is imperative to maintain the operation temperature of a device at optimum level (Viswanath *et al.* 2000). In the case of microprocessors for every increase of 10- 15°C in surface temperature, the risk of failure is doubled and therefore the lifespan of the device is halved (Belhardja *et al.* 2003). It should also be noted that as the complexity of microprocessor architecture continues there is an increased risk in the development of high localised power densities within the processor chip. These inequalities within the chip structure create an inhomogeneous temperature distribution which leads to localised hotspots as shown in Figure 1.2. Hotspots in microprocessors quite often induce a condition known as a thermal runaway. Thermal runaway is a phenomenon in electronics where as a device gets hotter it starts to draw more current, which generates more heat and in turn can produce temperatures high enough to melt the package (Belhardja *et al.* 2003).

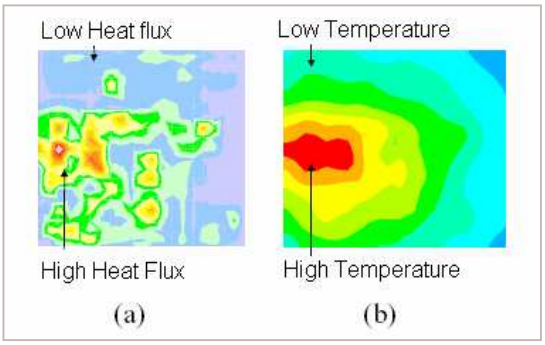

Figure 1.2 Shows the Heat Flux and Temperature distribution on the surface of a processor chip (Viswanath *et al.* 2000).

Consequently these giant leaps in microprocessor design providing more powerful, smaller and thus faster chips has placed a strong emphasis on the need for power conservation and new cooling technologies. For instance in may 2004 Intel announced that the thermal limits of their single core processors had been reached and that they would be abandoning two of their advance chip development projects in favour of obtaining more computer power from multiple processors working in parallel on a single chip (Markoff, 2004). This development route has also been followed by all the major chip manufactures and early this year the first quad core processor hit the

market. However even with these new developments, the problem of providing adequate heat removal from electronic devices has not been solved but merely eluded and therefore a question still remains “For how long?”.

The current cooling technology for microprocessors involves the conduction of heat from the surface of the silicon, through a thermal interface material[1], to a heat spreader (or external casing) and into a heat sink. From here the heat is removed through forced convection by a fan assisted ambient air stream. As you can see from the diagram shown in Figure 1.3, the heat conducted from the surface of the chip must travel a considerable distance before being removed by convection and often creates a substantial difference between the surface temperature of the chip and the surface temperature of the heat sink which leading to less than optimum cooling (Eason, 2005). Therefore in order to increase the cooling capacity of the system the distance between the chips surface and the air stream must be reduced.

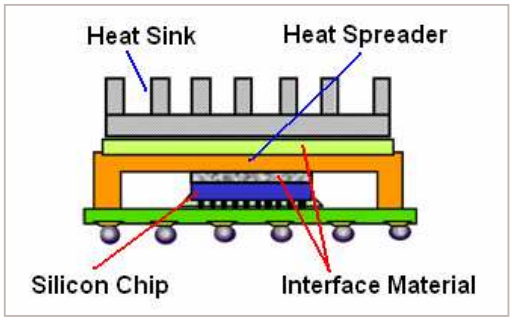

Figure 1.3 Conventional layout of an air cooled microprocessor (Viswanath *et al.* 2000).

One the most promising solutions to this problem is the incorporation of small flow passages known as microchannels[2] which would reduce the number of thermal interfaces and also the conductive heat path, providing a surface temperature closer to the chips actual temperature. Also according to Newton’s law of cooling *(Eqn. 2*) this increase in temperature would create a greater temperature change between the surface of the channels and the coolant flow stream and therefore increasing the heat transfer rate. A further increase in the heat transfer by an order of magnitude could also be accomplished by changing the coolant from air to water (Philips, 1990).

The application of such a system would involve cutting or etching a set of microchannel geometries either on the back of the silicon chip or on a separate structure, sealing the channels with a cover plate and attaching these passages to a continuous coolant flow.

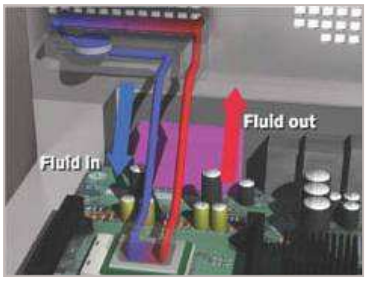

Figure 1.4 An example of a microchannel liquid cooling system (Cooligy, 2006).

[1] A grease, paste, oil or gel with a high thermal conductivity
[2] A flow passage with a hydraulic diameter (D_h) between 1mm and 1μm

An example of such a system is shown in Figure 1.4. Liquid cooling systems like this would provide a more than adequate means of cooling microprocessors with the current and predicted power densities.

In order to develop such a system it is imperative that the characteristics of microchannels are investigated. At present there has been quite a lot of research undertaken in this area of micro-mechanical engineering and therefore this project attempts to explore the forced convection liquid cooling of an electronic circuit, through microchannels which have been manufactured in silicon test samples. Experimental measurements of the heat transfer to a fluid (deionised water) and the pressure drop across two different types of microchannel test samples are to be performed based on methods derived in previous research (Eason, 2005). In the previous work the same characteristics were considered on a broader range of microchannel samples with different channel geometries and construction materials being used. In keeping with the recommendations of the former research, the existing test rig has been modified and also expanded to provide continuous data acquisition in order to significantly refine the results.

1.1. Objectives

- Prepare, assemble and calibrate the experimental test rig incorporating the recommended modifications.
- Develop a real time control programme using LabVIEW, to continuously record the necessary experimental measurements.
- Perform the pressure drop and heat transfer experiments on a number of microchannel test samples.
- Measure and calculate the average cross-sectional area of the microchannel test samples using Microscopic imagery, MATLAB and ProEngineer.
- Produce meaningful experimental results for both samples and compare these to known theoretical correlations effectively.

2.0 Literature Review

Convection liquid cooling has over the past 40 years continuously proven to provide a far superior means of heat removal from electronic systems in comparison to the conventional convection air cooling. However its research and development has suffered from a number of setbacks such as advances in transistor technology and the always favourable cost effectiveness of air cooling technology.

The history of liquid cooling for electronics dates as far back as 1964, when IBM introduced their first water cooling system to cool multiple stacks of electronic boards. Advances in water cooling technology continued for the next thirty years in order to cope with the continuing increase in the heat flux trend for the existing bipolar systems. In the mid-90's the development of CMOS technology provided a reduction in power dissipation by an order of magnitude in comparison to the existing bipolar systems and the thermal management for computers quickly shifted to the more cost effective air cooled convection systems. However this advantage has been short lived, as in space of ten years the newer CMOS technology has reached the maximum heat flux levels of the previous bipolar systems, as shown in Figure 2.1.

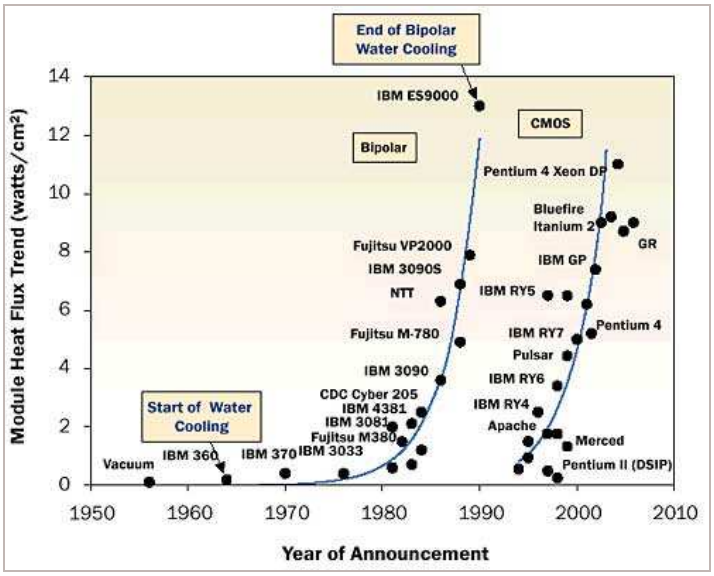

Figure 2.1 Details the increases in heat flux from computer processors over the past 60 years.

As stated earlier microchannels placed under forced convection liquid cooling is clearly the most efficient means of coping with the predicted heat generation from the future advances in computer microprocessors. The work of (Tuckerman and Pease, 1981) was the first to demonstrate such a system in operation. They concluded that a

power density of 790 W/cm^2, from a thin film resistor of 1cm^2 could be cooled to a maximum temperature of 71°C above the inlet fluid temperature (deionised water) using a compact array of microchannels etched into a silicon substrate with an anodically bonded Pyrex cover plate.

Ever since this first study by Tuckerman and Pease, there has been a considerable amount of research sustained in this field and as a result the heat transfer characteristics for a host of microchannels created in a range of materials with various shapes and sizes. Some of the manufacturing techniques and materials which have been used previously are; wet and dry etching (Silicon), electroplating (copper), Chemical Vapour Deposition (Diamond), and micromachining (for example sawing, milling, ultrasonic drilling, electro discharge machining and laser cutting) which can be used on most materials (Eason, 2005). Mostly, this research has produced channels of hydraulic diameter less than 1mm with a predominately circular channel shape, although rectangular, trapezoidal and square channels have also been tested. A more detailed explanation of the materials and manufacturing techniques used in the past can be found in the thesis of (Eason, 2005).

The fluid flow and heat transfer behaviour in microchannels has been compared and contrasted with conventional theory on numerous occasions. However, there have been considerable discrepancies between theoretical correlations and experimental measurements in many different publications. In the case of microchannel fluid flow, pressure drop experiments over a known length can be used to explore the validity of macroscale theory. From here, the product of the experimental friction factor and the Reynolds number is compared to corresponding constant from macroscale flow theory (Judy, J *et al,* 2002). However, many reports have claimed to prove and disprove the theory. Possible reasons for these inconsistencies have been attributed to *electrical double layer, surface roughness* and *aspect ratio* effects (Lee *et al* 2005)

In countless cases the measured experimental Nusselt number has been higher than the classic theoretical correlations for both laminar and turbulent flows. It was especially noticeable in the works of (Wu and Little, 1983; Bucci *et al*, 2003). In contrast there have also been reports showing experimental Nusselt numbers in good agreement with theoretical predictions, an example of which can be seen in the work of (Harms *et al,* 1999; Lee *et al,* 2004). And the same effect was also observed for the

heat transfer coefficients which were either too high or too low in comparison to theory. The transitional Reynolds's number from laminar to turbulent regions has also varied widely across different studies. As a result of all these varying results the modelling performance of the Navier-Stokes equations for heat transfer and pressure flow behaviour in microchannels has been challenged in numerous reports and also supported in others (Qu and Mudawar, 2002).

Papers by (Peng and Peterson, 1995a & 1995b) on single phase heat transfer in rectangular channels having different aspect ratios and hydraulic diameters, for laminar and turbulent flow systems. In the results the Nusselt number was found to be a function Reynolds and Prandtl number and also the aspect ratios. They also predicted the transition from laminar to turbulent began at lower Reynolds numbers in the same channels. These results accumulate to contradict the conventional theory.

On the opposing side, work by (Harms *et al* 1999) examined the heat transfer from rectangular channels of 251μm and 1000μm in width and length respectively and for the laminar flow regimes the experimental Nusselt Numbers agreed well with classic flow theory. Also experiments by (Qu and Mudawar, 2002), performed pressure drop and heat transfer measurements on rectangular channels of dimensions 231μm by 713μm subjected to a single phase laminar flow. The experimental results were in good agreement with the numerical solution of laminar Navier-Stokes equations thus validating the conventional theory for use in microchannels.

It is for this reason, the continuous proving and disproving of the conventional theory that the following experiment is being investigated as it is clearly evident that this field of research requires further study to resolve the complex means of accurately representing the experimental data from microchannel structures. In order to avoid some of the previous disparities recorded the experimental results will be compared to two different correlations one for Fully Developed flow and the second for simultaneously thermally and hydrodynamically developing. This should ensure both flow conditions are taken into account and therefore describe the flow system correctly. Also in literature there has also been regular disparities cause by the uncertainties created from the channel geometry and there fore the area of each channel shall be measured using an optical microscope with a high resolution CCD camera and points will be extracted from each channel image to accurately represent the channel geometry.

3.0 Theoretical Analysis

In this section the methods used to process the experimental data and the techniques used to discover theoretical results which correspond to this measured data are outlined in detail showing the equations implemented for each type of analysis. It should be noted that all calculations were completed using MATLAB programs written for the previous work, for more information on the result processing refer to section 6.0 and the attached CD.

3.1. Experimental Theory

In the case of the experimental analysis, measured data the pressure drop (P_L), the mass flow rate ($\dot{m}$), the cross sectional area (A *or* A_{Theory}) and the surface area of the channels (A_T) required no further adjustment as the measurements are taken in standard units (SI). For the temperature readings an average value for the inlet and outlet conditions was calculated. Once an average fluid temperature was determined thefluid properties were calculated at this temperature using the *water_prop.m* and the mean velocity (u) of the fluid in the channels was calculated using Equation 1.

$$u = \frac{\dot{m}}{n\rho_{TavgF} A_{Theory}} \qquad \textit{(Eqn. 1)}$$

This velocity was then used to calculated the Reynolds number (Equation 2) and hence establish if the fluid flow was turbulent or laminar.

$$\mathrm{Re} = \frac{\rho_{TavgF} u D_h}{\mu_{TavgF}} \qquad \textit{(Eqn. 2)}$$

In order to represent the heat transfer characteristics of the system the convective heat transfer coefficient (h) was calculated (Eqn. 4) from *Newton's Law of Cooling* (*Eqn. 3*). These equations are calculated using the total surface area of the channels where convection takes place (A_t), for the both channel types channels this area was assumed to be the surface area of the silicon walls not including the glass cover wall.

$$Q = \dot{m} c_P \left(T_{outF} - T_{inF}\right) = h A_t \left(T_{avgS} - T_{avgF}\right) \qquad \textit{(Eqn. 3)}$$

$$h = \frac{\dot{m} c_{P_{TavgF}} \left(T_{outF} - T_{inF}\right)}{A_t \left(T_{avgS} - T_{avgF}\right)} \qquad \textit{(Eqn. 4)}$$

This convective heat transfer coefficient was the transformed to a more meaningful non-dimensional value known as the Nusselt Number (*Eqn. 5*), which is calculated using the hydraulic diameter (D_h) of the channel (*Eqn. 6).*

$$Nu = \frac{hD_h}{k_{TavgF}} \qquad \textit{(Eqn. 5)}$$

$$D_h = {}^{4A}\!\diagup_{Wetted\ Perimeter} \qquad \textit{(Eqn. 6)}$$

The uncertainty of these experimental values was calculated using the direct method as shown in section 3.4.1.

3.2. Theoretical Calculations

The experimental results shown in section 7.0 were compared to two different theoretical correlations. The first was taken from (Rohsenow *et al* 1985) and is based on the calculations of (Shah and London 1978) & (Schmidt, 1978) for standard fully developed laminar flow through rectangular and trapezoidal ducts with constant heat flux wall conditions. The second is taken from the work of (Muzychka and Yovanavich 2004) where the square root of the cross sectional area and the aspect ratio (ε) of a channel are used to calculate the heat transfer characteristics of the channels for combined thermally and hydrodynamically developing flow conditions.

3.2.1. Theoretical Pressure Drop

In both correlations the theoretical pressure drop across the channels was derived for each experimental data point using Darcy's equation, as shown in (*Eqn. 7*).

$$P_L = f\frac{4L}{D_h}\frac{\rho u^2}{2} \qquad \textit{(Eqn. 7)}$$

This formula was also used to calculate the pressure drop in the manifolds between the pressure tappings and the channels entrance and exit points. In to order calculate the pressure drop for both the manifolds and the microchannels, the Fanning Friction Factor (*f*) was used, which is inversely proportional to the Reynolds number for fully developed flow. As shown in section 6.2, the pressure drop is proportional to the reciprocal of the cross sectional area squared and therefore it was extremely important to measure the channel dimensions accurately as small changes in these dimensions would cause large changes in the pressure drop across the channels. If this was the

case, deviations between the experimental and theoretical readings would be observed in the results.

3.2.2. Rohsenow Correlation

For the Rohsenow correlation the *fRe* values for the rectangular and trapezoidal channels with fully developed laminar flow were taken for the data by (Shah and London 1978) as shown in Table 3.1 & Table 3.2 respectively. The friction factor was then found by dividing these values by the corresponding Reynolds Number for each data point. For the rectangular channels the *fRe* values are displayed as a function of the aspect ratio of the channel (commonly taken as the channel width over is height ($^{W}/_{H}$) and ranges between 0 and 1). In the case of the trapezoidal channel the *fRe* values were outlined as a function of the acute corner angle (ϕ, as shown in Figure 3.1) for different degrees.

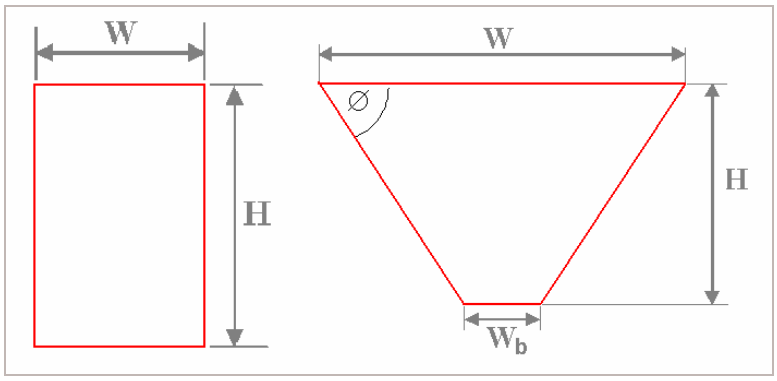

Figure 3.1 Shows the Channel Shapes with the dimensions used for the experiments.

The resultant friction factor could then be used to discover the theoretical pressure drop across each type of channel using Equation 7.

Table 3.1 Shows the Friction Factor - Reynolds Number as a function of the aspect ratio for a rectangular duct with fully developed laminar flow (Rohsenow *et al* 1985).

Aspect Ratio	***fRe***	***Aspect Ratio***	***fRe***	***Aspect Ratio***	***fRe***
1	14.22708	0.5	15.54806	1/9	20.90385
0.9	14.26098	0.4	16.3681	0.1	21.16888
1/1.2	14.32808	1/3	17.08967	1/12	21.58327
0.8	14.3778	0.3	17.51209	1/15	22.01891
0.75	14.4757	0.25	18.23278	0.05	22.47701
1/1.4	14.56482	0.2	19.0705	0.02	23.3625
0.7	14.60538	1/6	19.7022	0	24
2/3	14.71184	1/7	20.1931		
0.6	14.97996	0.125	20.58464		

To represent the heat transfer characteristics of the system the experimental temperature data must first be examined to determine if the system is a constant surface temperature or constant heat flux system. As shown in Figure 3.2 a constant surface temperature system starts off at the inlet with a large temperature difference between the surface and the fluid and at the outlet the difference is minimised as temperature of the fluid increases. For the constant heat flux system, the temperature difference between the surface and the fluid remains constant throughout, and therefore both temperatures increase at a constant rate between the inlet and the outlet points. From the initial temperature data the system clearly behaved like it was a constant heat flux system and therefore all correlation data must correspond to this condition.

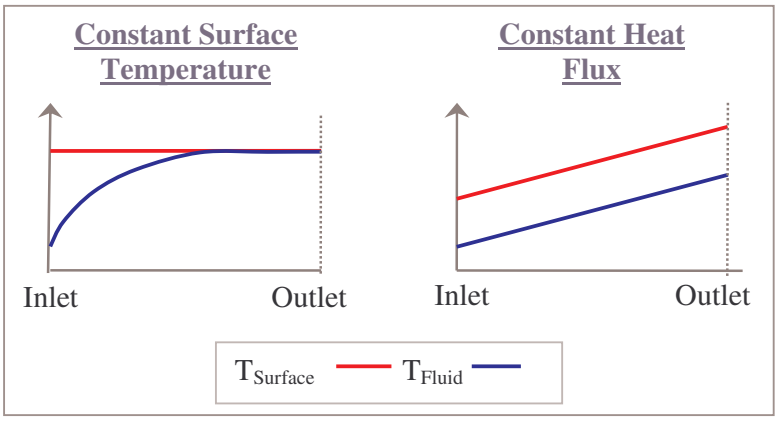

Figure 3.2 Demonstrates the different temperature profiles for the Constant Surface Temperature and Constant Heat Flux (Eason, 2005).

To establish the theoretical Nusselt number for each data set correlation data by (Schmidt, 1978; Shah and London 1978) were consulted for the rectangular (Table 3.3) and trapezoidal (Table 3.2) channels respectively.

Table 3.2 Shows the Friction Factor - Reynolds number and the Nusselt number for fully developed laminar flow as a function of the acute corner angle and aspect ratio in a trapezoidal duct (Rohsenow *et al* 1985).

H/Wb	*fRe*	*Nu*	*fRe*	*Nu*	*fRe*	*Nu*	*fRe*	*Nu*	*fRe*	*Nu*
	ø = 85°		**ø = 75°**		**ø = 60°**		**ø = 45°**		**ø = 30°**	
∞	12.474	2.446	13.065	2.91	13.333	3.111	13.153	2.982	12.744	2.68
8	17.474	4.366	14.907	3.52	13.867	3.284	13.301	3.03	12.76	2.697
4	16.74	4.483	14.959	3.72	13.916	3.348	13.323	3.048	12.782	2.704
2	15.015	3.896	14.34	3.61	13.804	3.35	13.364	3.081	12.875	2.736
4/3	14.312	3.636	14.118	3.542	13.888	3.39	13.541	3.155	13.012	2.919
1	14.235	3.608	14.252	3.594	14.151	3.495	13.827	3.268	13.246	2.821
3/4	14.576	3.736	14.697	3.766	14.637	3.691	14.26	3.469	13.599	3.077
1/2	15.676	4.175	15.804	4.219	15.963	4.14	15.206	3.888	14.323	3.436
1/4	18.297	5.363	18.303	5.317	18.053	5.247	17.397	4.943	16.284	4.349
1/8	20.599	6.501	20.556	6.482	20.304	6.341	19.743	6.034	18.479	5.569
0	24	8.235	24	8.235	24	8.235	24	8.235	24	8.235

From these standard correlations, a constant Nusselt number value for each channel type was determined by linearly interpolating between the measured channel characteristics (ε and Φ) used to define the Nusselt number.

Table 3.3 Shows the Nusselt Number as a function of the aspect ratio for fully developed laminar flow in a rectangular channel with three walls transferring heat at a constant heat flux (Rohsenow *et al* 1985).

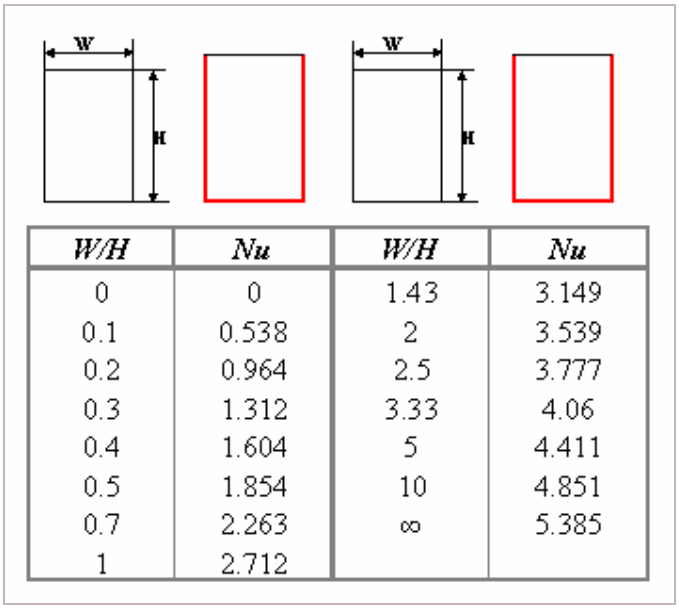

W/H	*Nu*	*W/H*	*Nu*
0	0	1.43	3.149
0.1	0.538	2	3.539
0.2	0.964	2.5	3.777
0.3	1.312	3.33	4.06
0.4	1.604	5	4.411
0.5	1.854	10	4.851
0.7	2.263	∞	5.385
1	2.712		

3.2.3. Muzychka and Yovanovich Correlation

For the Muzychka and Yovanovich correlation, the friction factors were calculated using the cross sectional area of the duct as the characteristic dimension rather than the hydraulic diameter. This method was confirmed in the paper (Muzychka and Yovanovich, 2004) by comparing their results to the findings of Shah and London. This theory was also arrived at in the research of constructal theory of organization in nature by (Bejan, 2000). In order to find the friction factor for this method the aspect ratio was first calculated as follows

$$\varepsilon = \frac{W}{H} or \frac{H}{W}, 0.1 < \varepsilon < 1 \qquad \textit{(Eqn. 8)}$$

In Equation 8, the two methods which can be used to ensure the aspect ratio is between the given range are shown, however in these experiments the $^{W}/_{H}$ method was more than adequate in both cases (These dimensions can be seen in Figure 3.1). The 0.01< ε <1 was particularly important for the rectangular ducts which behave more like parallel plates below an aspect ratio of 0.01. Once the aspect ratio was determined a dimensionless length for the channels was calculated from Equation 9.

$$z^+ = \frac{L}{\sqrt{A}\,\mathrm{Re}_{\sqrt{A}}} \qquad \textit{(Eqn. 9)}$$

The friction factor can then be calculated using the *fRe* values for fully developed flow provided by Equation 10 and also the apparent friction factor (f_{app}), which accounts for developing flow effects at the entrance region of the channels can be calculated using Equation 11.

$$f\,\mathrm{Re}_{\sqrt{A}} = \frac{12}{\sqrt{\varepsilon}(1+\varepsilon)\left[1 - \frac{192\varepsilon}{\pi^5}\tanh\left(\frac{\pi}{2\varepsilon}\right)\right]} \qquad \textit{(Eqn. 10)}$$

$$f_{app}\,\mathrm{Re}_{\sqrt{A}} = \left[\left(f\,\mathrm{Re}_{\sqrt{A}}\right)^2 + \left(\frac{3.44}{\sqrt{z^+}}\right)^2\right]^{\frac{1}{2}} \qquad \textit{(Eqn. 11)}$$

It should also be noted that the Reynolds number is calculated using the square root of the cross sectional area as shown in Equation 12.

$$\mathrm{Re}_{\sqrt{A}} = \frac{\rho u\sqrt{A}}{\mu} \qquad \textit{(Eqn. 12)}$$

The Nusselt number correlation from (Muzychka and Yovanovich, 2004) was derived for combined thermally and hydrodynamically developing flow. It is also based on the square root of the CSA, but it does not cater for any other wall heating conditions other than all walls heated. However it has been claimed to work well for all non-circular ducts such as rectangular and trapezoidal ducts in the past. The correlation accounts for the thermally developing conditions through the variation in the Prandtl number as shown in equation 13.

$$f(\mathrm{Pr}) = \frac{B_1}{\left[1 + \left(B_2\,\mathrm{Pr}^{1/6}\right)^{\frac{9}{2}}\right]^{\frac{2}{9}}}, 0.1 < \mathrm{Pr} < \infty \qquad \textit{(Eqn. 13)}$$

Another dimensionless length (Equation 14) which incorporates the Prandtl number is also required for the Nusselt number correlation shown in Equation 15.

$$z^* = \frac{L}{\sqrt{A}\,\mathrm{Re}_{\sqrt{A}}\,\mathrm{Pr}} \qquad \textit{(Eqn.14)}$$

$$Nu_{Muzy}\left[\left(\frac{C_4 f(\mathrm{Pr})}{\sqrt{z^*}}\right)^M + \left(\left\{C_2 C_3\left(\frac{f\,\mathrm{Re}_{\sqrt{A}}}{z^*}\right)^{1/3}\right\}^5 + \left\{C_1\left(\frac{f\,\mathrm{Re}_{\sqrt{A}}}{8\sqrt{\pi}\varepsilon^{\gamma}}\right)\right\}^5\right)^{\frac{M}{5}}\right]^{\frac{1}{M}}$$

(Eqn. 15)

The correlation can model the heat transfer characteristics of any simultaneously developing flow in a duct of arbitrary cross section (Muzychka and Yovanovich, 2004). This correlation also make use of a simple linear approximation (*M*) known as the blending parameter (Equation 16) which accounts for the variations in geometries and data. The constants used for the previous equation can all be found in Table 3.4 taken from (Muzychka and Yovanovich, 2004).

$$M = 2.27 + 1.65\,\mathrm{Pr}^{\frac{1}{3}} \qquad \textit{(Eqn.16)}$$

Table 3.4 Details the constants used for the Muzychka and Yovanovich correlation.

	B1	***B2***	***C1***	***C3***
Uniform Wall Temp	0.564	1.664	3.24	0.409
Uniform Heat Flux	0.886	1.909	3.86	0.501
	C2	***C4***		**γ**
Local	1	1	**Upper**	1/10
Average	3/2	2	**Lower**	-3/10

3.3. Entrance and Exit Losses

As the pressure tappings used to measure the pressure drop across the channels had to be located outside the channels, it was therefore necessary to account for the pressure losses due to the sudden expansion and contraction of the fluid as it passes through the entrance and exits of the microchannels. In order to provide accurate theoretical pressure drop results the flow friction losses caused by the manifold must also be taken into consideration. The following equation shown in matrix form shows the equations used to calculate the inlet and outlet pressure drop losses.

$$\begin{bmatrix} P_{Li} \\ -P_{Lo} \end{bmatrix} = \frac{\rho u^2}{2}\left[\left(1-\left(\frac{A_2}{A_1}\right)^2\right) + \begin{bmatrix} K_c \\ -K_e \end{bmatrix}\right] \qquad \textit{(Eqn. 17)}$$

The area ratio in equation 17 places the final cross sectional area (A_1) over the initial cross sectional area (A_2) and the loss coefficients K_c & K_e are taken from Figure 3.3

which details these coefficients for laminar flow through an abrupt entry or exit of a square duct.

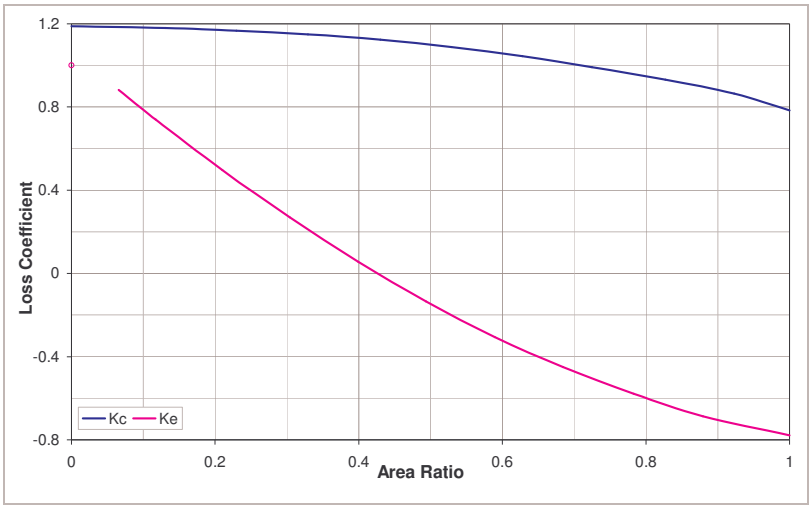

Figure 3.3 Details the loss coefficients for laminar flow through an abrupt entry and exit from of a square duct (Eason *et al* 2007).

3.4. Uncertainty

Experimental uncertainty measures the accuracy of the equipment, the measurement techniques and also the calculations used in an experiment to determine the overall effect on the results of the experiment. As result of this, three set of results are required for all experiments; the nominal, the upper and the lower results. The upper and lower results are usually displayed in the form of extra curves or error bars in a result plot and in effect the measure values could lie at any point between these two values.

3.4.1. Experimental Uncertainty

For these experiments the method used to calculate the uncertainty was the direct method as it is the most conservative method which often returns large uncertainty values. The method is quite simple and involves three calculations as shown below.

Measured values: $A = 25 \pm 0.5$ & $B = 65 \pm 4$

The Required *Result is = A x B* and therefore the *Nominal result = 25 x 65 = 1625*, the *Upper Result = 25.5 x 69 =1759.5* & the *Lower Result = 24.5 x 61 =1494.5.*

Therefore the direct uncertainty result is ***1625 +134.5/130.5***

It should be noted that it is extremely unlikely that both uncertain terms would be at their maximum or minimum at the same time and so the chances of the actual

uncertainty of an experiment reaching this maximum or minimum level are exceptionally low and therefore the experimental data would lie within this region.

3.4.2. Theoretical Uncertainty & Statistical Methods

The theoretical uncertainty calculated for the work was the uncertainty of the channel measurements. To calculate the uncertainty for a range of data, a sample standard deviation was taken using Equation 18.

$$\sigma_x = \sqrt{\frac{\sum_{i=1}^{n}(x_i - \bar{x})^2}{n-1}} \qquad \textit{(Eqn. 18)}$$

A sample standard deviation is used mainly for instances where only a sample of measurements is taken rather than all measurements being taken. For example only 6 of the 22 channels were measured completely according to the procedure described in section 4.9. As there was no guarantee that the channel cross sectional area remained constant along the channel, a sample standard deviation was used to provide a more suitable representation of the variation in the measurements.

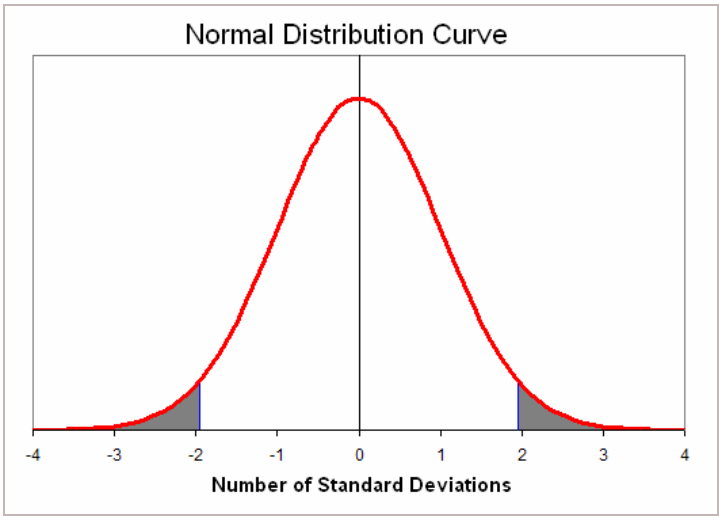

Figure 3.4 Shows a normal distribution curve with a 95% confidence interval (clear region under curve) calculated from ±1.96 standard devations.

A normal distribution as shown in Figure 3.4 plots all the data results for a data set under the curve with a number of standard deviations on either side of the averaged result. For this application a symmetrical 95% confidence interval (CI) (clear region of Figure 3.4) was required and so the standard deviation of all the results was multiplied by 1.96, creating the ± uncertainty for the average result. Therefore, there was a 95% probability that all of the results will be found within the nominal value (averaged result) ± 1.96 standard deviations.

4.0 Experimental Apparatus

The following chapter details the design (Eason, 2005) and specification of the test rig used during the experiments described in section 0. Details of the individual components and there calibration have also been included along with the methods used for data acquisition and the recommended modifications from the previous work of (Eason, 2005).

4.1. The Microchannel Test Rig

The requirements of the system were to provide steady fluid flow through the microchannel test samples over a range of Reynolds numbers (Re) In these experiments the upper Re limit of 350 was set by the pressure transducer. In order to provide accurate results, the system was also required to accommodate a means of mass flow rate, pressure, and temperature measurement as well as data acquisition using LabVIEW software. During testing it is important to keep the change inlet fluid temperature as low as possible and so in addition to the original design incorporating a reservoir with a large volume; a cooling radiator has been added. The large capacity reservoir minimises increases in the fluid temperature due to the huge volume of coolant fluid and relatively small amount of heat added to the coolant.

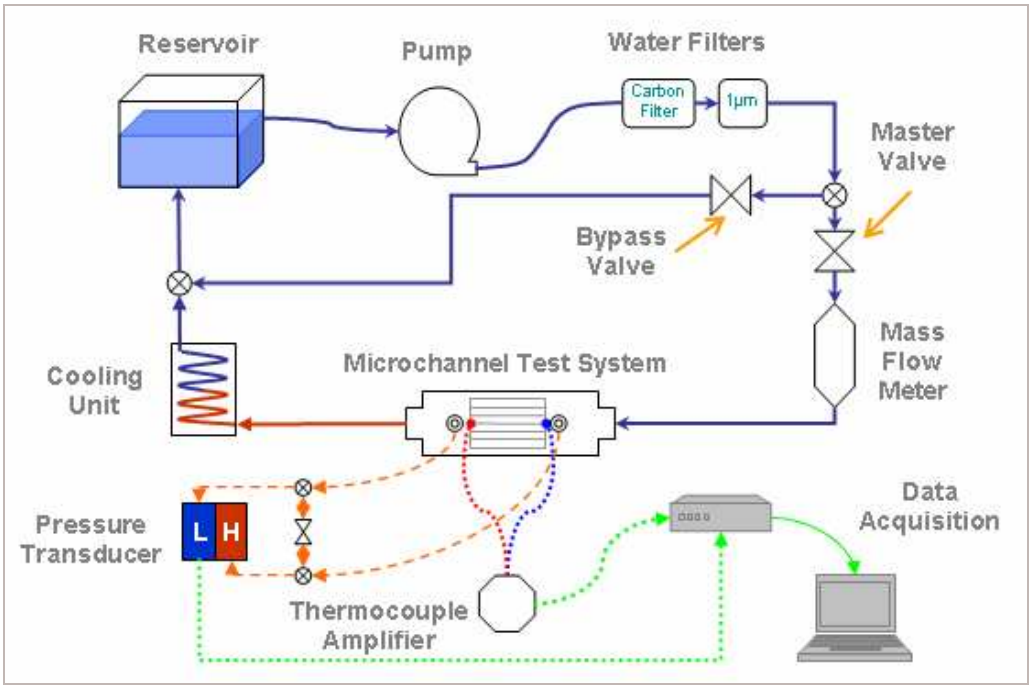

Figure 4.1 Details the layout of the microchannel test rig

For the majority of testing simple natural convection through the surface area of the radiator and the reservoir provided sufficient cooling to the fluid, further cooling could be administered by placing the radiator in a temperature controlled cooling bath.

A schematic drawing of the microchannel test rig used for experimental testing is shown above in Figure 4.1. The devices within the test rig are connected using 4mm inside diameter (ID) FEP tubing and Swaglok fittings with Vespel ferrules, as shown in Figure 4.2. These fittings prevent leakage and allow modifications to the flow loop to be performed relatively quickly using a spanner to make and break connections.

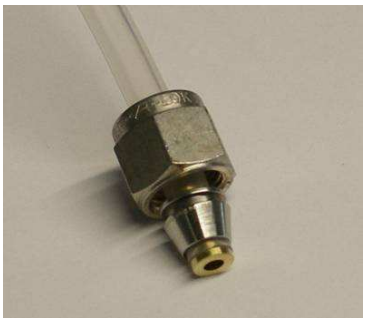

Figure 4.2 Shows the Swaglok Fitting and Vespel ferrule set up.

4.2. Microchannel Test Samples

In this experiment the characteristics of rectangular and trapezoidal microchannels manufactured in silicon were investigated. Both samples were manufactured in the previous work by (Eason, 2005) and contain an array of 22 channels manufactured in silicon substrate over a nominal area of 15 by 30 mm; both samples are sealed with a Pyrex glass to complete the structure.

The rectangular channels were manufactured using Deep Reactive Ion Etching (DRIE) process and were spaced approximately 400μm apart with a target depth and width of 320μm and 300μm respectively, as illustrated in Figure 4.3. For these samples a 100mm diameter silicon wafer was used and from this, six microchannels samples were produced. The silicon wafer is first baked for 40 minutes at 250°C, to prepare the surface of the silicon for a layer of photoresist (light sensitive chemical - SPR 220) which was then allowed to harden. A photolithography mask containing the outline of the desired channels was placed over the wafer and subsequently exposed Ultra Violet (UV) light. The UV light breaks down the exposed photoresist allowing it to be removed and thus leaving

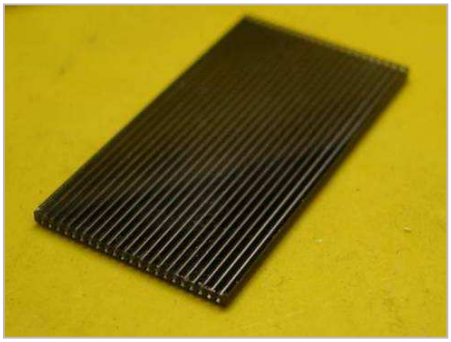

Figure 4.3 An example of a DRIE microchannel sample.

the mask outline of the required channels exposed on the silicon surface. The remaining photoresist protects the silicon from the DRIE process, leaving only the necessary surfaces exposed to its effects. The DRIE process bombards the silicon surface with ions flowing at a high speed for a set length of time (to produce the required depth), these ions then collide with the surface breaking off layers of silicon with an isotropic component speeding the etch rate, while an anisotropic component creates near vertical channel walls (Eason, 2005).

The remaining photoresist can then be removed from the surface of the silicon allowing the structure to be cleaned and dried in an oven. The silicon wafer was then aligned with an extremely smooth sheet of Pyrex glass, both pieces clamped together and heated to 400°C while a voltage of 1000-1500 volts was forced through the glass and silicon. This voltage then drives sodium (Na) ions from the glass into the silicon surface creating an irreversible bond between both materials thus completing the channel. The six samples are then cut out of the wafer in two stages using the correct dicing blade for each layer of material.

For the trapezoidal channels, shown in Figure 4.4 which are created in silicon with a wet etch process using Potassium Hydroxide (KOH), this process etches silicon in a anisotropic manner, meaning it does not remove the silicon particles at the same rate in all directions. The different planes in a crystal structure are described by a Miller Index. Miller indices are found by discovering the points at which the crystal plane intersects with each axis *(x, y* and *z)* and taking the reciprocal of these, for example intersect points of (3,0,0), (0,9,0) and (0,0,6), give the reciprocal of ($^1/_3$, $^1/_9$, $^1/_6$). These fractions are then reduced by multiplying across by the lowest common factor (in this case 18) to produce a Miller index of (6,2,3). If the crystal plane is parallel to a specific axis it is simply given an intersection of ∞, which will produce a miller index number of zero for the corresponding axis. Negative intersected planes are shown with an macron as follows, $\bar{1}$ (Dutch, 1997). The silicon wafers used for these samples were made from a single continuous silicon crystal, and so is the crystal alignment remains consistent

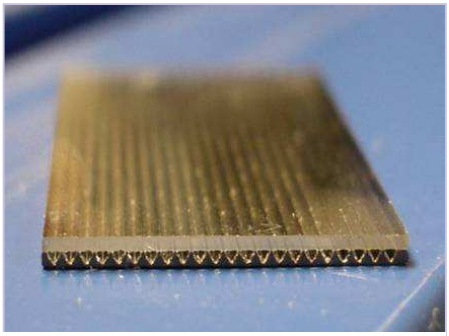

Figure 4.4 An example of the wet etched microchannel test sample

throughout the wafer. In this case a (100) silicon wafer with a diameter of 100mm was used to create 8 test samples.

Before the channel manufacture the silicon wafer must first be aligned by etching some test marks, to ensure the etching takes place in the required planes. This process involved first oxidising the wafers surface in a furnace and covering the whole wafer in a layer of Silicon Nitride (Si_3N_4), the first layer of silicon dioxide prevents the protective Si_3N_4 layer from peeling during the wet etching process. Once this has been completed a 1.1μm layer of photoresist is spread over the top surface and the alignment mask then placed over the wafer exposing only the required points to UV light. The weakened photoresist can then removed along with the underlying layers of Si_3N_4 (using a dry plasma etch) and silicon dioxide (with a 10:1 deionised water and Hydrofluoric acid solution). The wafer was then placed in a KOH bath and the exposed silicon etched to a depth of 14μm. The trapezoidal channels are etched in the very same manner; however this time the overall mask outline was used which was aligned to the previously etched test marks. The resultant structure contains an array of 22 channels to a depth of 400μm with a maximum width of 585μm which a pitch of 690μm. The remaining layers of photoresist, Si_3N_4 and silicon dioxide were then removed and the wafer was cleaned. The microchannels are then completed by anodically bonding the Pyrex glass sheet to the upper silicon surface and cutting out the individual samples as described previously. Further information on the design and manufacturing processes can be found in (Eason, 2005).

4.3. The Microchannel Test System

The microchannel test system used for the experiments had five main requirements, to provide a means of holding various different samples, allow axial fluid flow through the samples, provide an adequate area for the heat load application and finally present a means measuring the pressure drop across the test pieces and the temperature in both the inlet and outlet manifolds.

An exploded view of the various components in the microchannel test system is shown in

Figure 4.5. The components labelled in the diagram are as follows (1 & 2) the cover plate and glass insert which has since been replaced as a single Perspex cover, (3) the double layer silicone gasket, (4) microchannel test sample, (5) interchangeable

aluminium shims, (6) Aluminium manifold block, (7) Pressure tapping manifold, (8) PTFE tape gasket for pressure tapping manifold, (9) the 4mm inlet tubing & connection fitting, (10) 1/16" connection fitting to the pressure transducer.

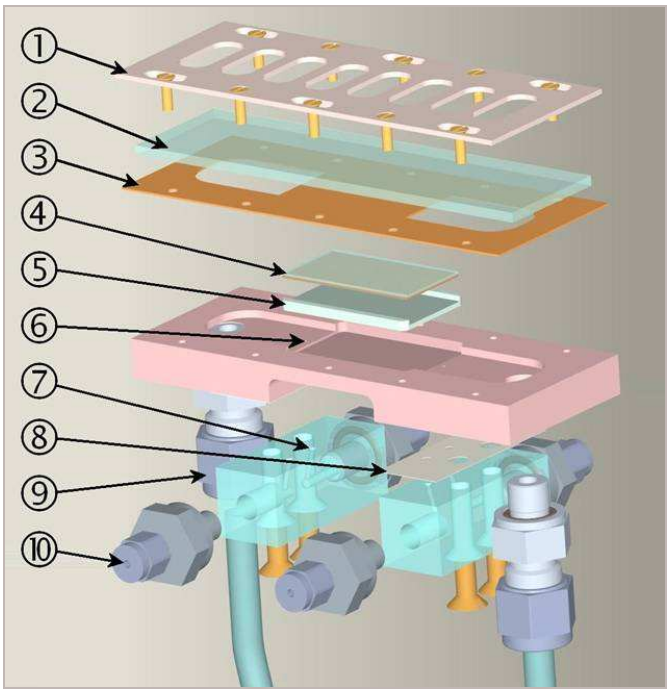

Figure 4.5 Details the various components of the microchannel test system (Eason, 2005).

The interchangeable aluminium shims are designed to compensate for the changes in the dimensions of different types of samples and thus provide a precise seal around the sample. It should also be noted that the six thermocouples used for temperature measurement in the inlet and outlet manifolds were simply passed between the two silicone gaskets which provided an appropriate seal around the 127μm diameter bare thermocouple wire.

4.3.1. Heating System

Heating is applied to the microchannel test sample from three aluminium bodied power resistors (Farnell 9506861) mounted on the aluminium manifold using a high temperature thermal epoxy, rated to 120°C. The three heater resistors are located in between the two pressure tapping manifolds on the back of the aluminium manifold block and cover a surface area of 7cm^2. The three

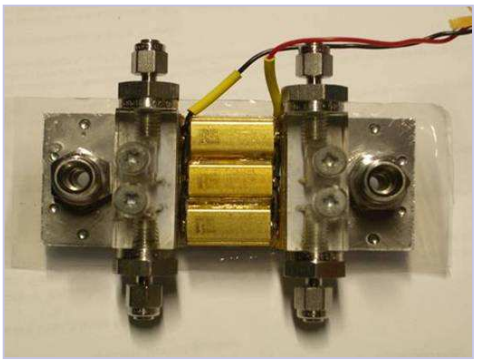

Figure 4.6 Shows the three heating resistors mounted on the aluminium manifold.

resistors were wired in parallel and each resistor was rated to dissipate 15W of power using simply air cooling, (Eason, 2005). In these experiments the maximum power was limited by the power supply which provided a maximum output of 15.93V at 3A or 47.79W. This power output gives a power density of 6.83W/cm^2 from the resistors, which is approximately 11.2% and 9.2% of the 2007 International Technology Roadmap for Semiconductors (ITRS) predictions for the high and cost performance chips respectively.

4.4. Pumping System

The fluid flow in these experiments was provided by a speed controlled Tuthill electric motor (V2DC00S00000) which in turn magnetically drives a Tuthill gear pump (DDS.19PPPV2NM00000), as shown in Figure 4.7. The system displaces 0.19ml per revolution and has an operating range of 60 to 3600rpm in increments of 10rpm. The unit has an internal feedback control loop and provides a constant pump speed regardless of the load. The speed of the pump was controlled externally through the data acquisition software with input of 0–10 Volts, a conversion constant (which was found to be 365.5 through trial and error) was necessary to provide an accurate representation of the actual motor speed on the LabVIEW control program display.

Figure 4.7 An internal view of the gear pump and the assembled system & motor.

4.4.1. Filtration

Due to the difficulties with channel clogging in the previous work (Eason, 2005), two separate filters have been incorporated into the system. A 1μm Whatman polycap filter (36 HD 6703 – 3610) was used to restrict solid particles passing through the microchannels while a Whatman carbon cap (6704 – 1500, which is an activated carbon filter) removed all organic contaminants from the coolant. To install the filters into the test rig they must first be filled with water making use of the bleed cap to remove any trapped air in the filter.

4.5. Mass Flow Measurement

The mass flow measurements for the system were taken using a Bronkhurst Liquiflow L30 mass flow meter. The unit provides no obstruction to the fluid flow as it calculates the mass flow rate by measuring how much heat energy is needed to maintain a constant temperature rise in the fluid flowing through the mass flow meter. The flow meter is calibrated to within ± 1% of 10kg/hr its quoted maximum flow rate but in fact the highest measurement observed was 10.62kg/hr. The mass flow meter outputs a 0–10V signal, and so before the signal can be logged as a mass flow rate by the control program a calibration constant must be acquired.

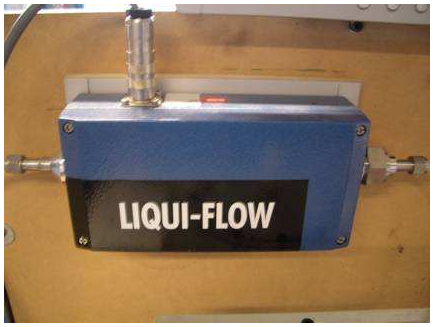

Figure 4.8 Details the Bronkhurst Liquiflow L30 mass flow meter.

4.5.1. Mass Flow Calibration

To discover the calibration constant a simple test measuring the flow rate and the output voltage from the Liquiflow L30 over the operating range of the pump was performed. The first step was to set the pump speed and allow the fluid flow to reach a steady state. Once this has been achieved the fluid flow was collected in a plastic cup over a timed period of one minute, this was performed using a digital quartz stopwatch with an accuracy of ±0.5sec with this method of measurement. During this timed period an average of the mass flow meter voltage was also taken from the control program. Once this measurement was completed the plastic cup and water were weighed on a Satorius BL150S Digital Balance, it is important to make sure that the scale had been offset to account for the weight of the cup. The Digital Balance can measure mass up to 150g with an uncertainty of ± 0.08g, however with the weight of the cup offset the max measurement was reduced to almost 110g. The following steps were then repeated for different flow rates and the results were used to plot the mass flow rate (g/min) against the output voltage from the mass flow meter with a linear trendline fitted as shown in Figure 4.9. The trendline is set to pass through the origin and the slope of the line 16.743 g/min per volt provides the required calibration constant.

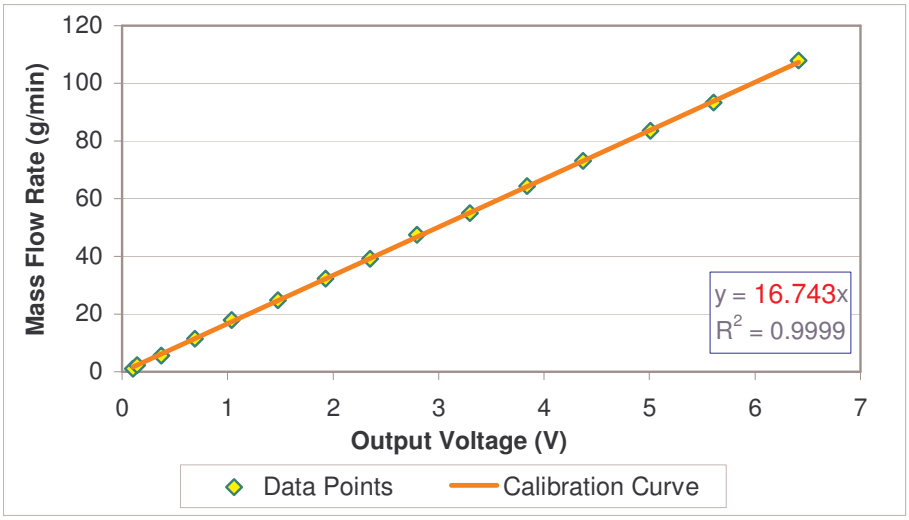

Figure 4.9 Details the results of the mass flow meter calibration

4.6. Pressure Drop Measurement

The pressure drop across the microchannel test samples was taken from 0.5mm diameter tappings located in the centre of the inlet and outlet manifolds, at a distance 1.5mm and 3mm from the entrance and exit of the microchannels respectively. Pressure changes in the manifolds were measured using a Setra (model no. 2301001PD2F2EBC) differential pressure transducer rated to 6.89kPa (1 PSI) ± 0.25% via the pressure manifold block and 1/16" tubing (Eason *et al,* 2007). The high and low pressure tubes were linked using a flexible tube as a crossover valve, which could be opened and closed using a clothes peg or an elastic band, to protect the transducer diaphragm from any overloading conditions. The crossover valve and pressure transducer are shown in Figure 4.10. The measured pressure difference in the system was represented by an output voltage (0-10V) from the transducer and was sent to the control program for processing and data acquisition, again calibration was required to calculate a conversion constant to represent this voltage as a pressure (Pa).

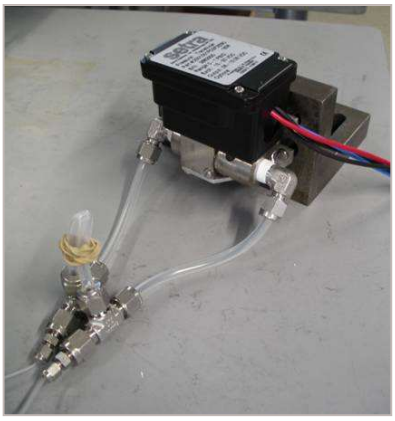

Figure 4.10 The Setra Pressure Transducer and Crossover valve.

Before any experiments took place it was imperative that any air in the transducer and the connection lines was removed. To clear the connection tubes the pump was run at full speed with the crossover valve open so that any presence of air in the lines

would simply be pushed out the outlet manifold of the microchannel test system. To remove the air from the pressure transducer the following steps were performed.

- The bleed port screw for the high pressure chamber was loosened by approximately one and a half turns, with the crossover valve open and the pump running at a high speed. The outflow of fluid was absorbed using some tissue.
- The transducer was then held so that the bleed port was higher than the rest of the chamber, allowing any air bubbles to escape. The body of the transducer and the crossover valves were also lightly tapped to dislodge any smaller bubbles trapped inside.
- Once the evidence of air escaping was no longer present the screw valve was closed and the same procedure was used on the low pressure chamber until all air had been removed.
- The whole process was repeated, to ensure the all pressure measurements were not altered by the presence of air in the pressure chambers.

It should also be noted that during the initial experiments it was discovered that quite a lot of noise was induced into the pressure output signal from the pump motor vibration and therefore the pressure transducer and the crossover valve were moved to a separate table and placed on a damping cushion to reduce this undesired effect.

4.6.1. Pressure Transducer Calibration

In order to calculate a calibration constant for the output voltage from the pressure transducer, a known pressure is applied to the high pressure chamber and the output voltage is recorded. This was achieved using two long graduated burettes, which were connected to the pressure transducer via the crossover valve and gradually filling one burette with water to generate an increase in pressure. It is important to note that small changes in the vertical position of the burette produced variations in pressure and therefore before calibration each burette was tested using a spirit level to ensure they were fully vertical. The calibration process is as follows.

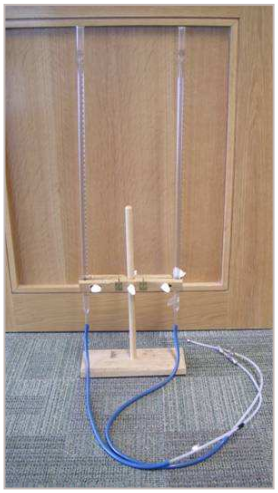

Figure 4.11 Shows the burettes used for calibration.

1) The pressure transducer and crossover valve were disconnected from the test system and attached too the burettes, and some water was added to the circuit making sure water flowed from one burette to the other.

2) If any air bubbles were present in the circuit the levels in both burettes were seen to be unequal. If this was the case more water was added to one burette, thus forcing any air bubbles in the connection lines out the other burette. If the water levels were still unequal the pressure transducer was bled again as previously described.

3) Once the set-up was complete and the pressure was equal on both sides, the crossover valve was closed and the pressure transducer output signal was zeroed automatically in the LabVIEW control program.

4) To apply a known pressure, water was added in stages to the burette connected to the high pressure chamber and the following equation $P = \rho gh$ was used to calculate the pressure acting on the transducer.

5) At each stage the height of the fluid and the output voltage was recorded, however the burettes were graduated in ml not mm and so a vernier callipers was used to measure the distance between a couple of graduations to provide an average distance between each marking on the scale, the result of which can be seen inFigure 4.12.

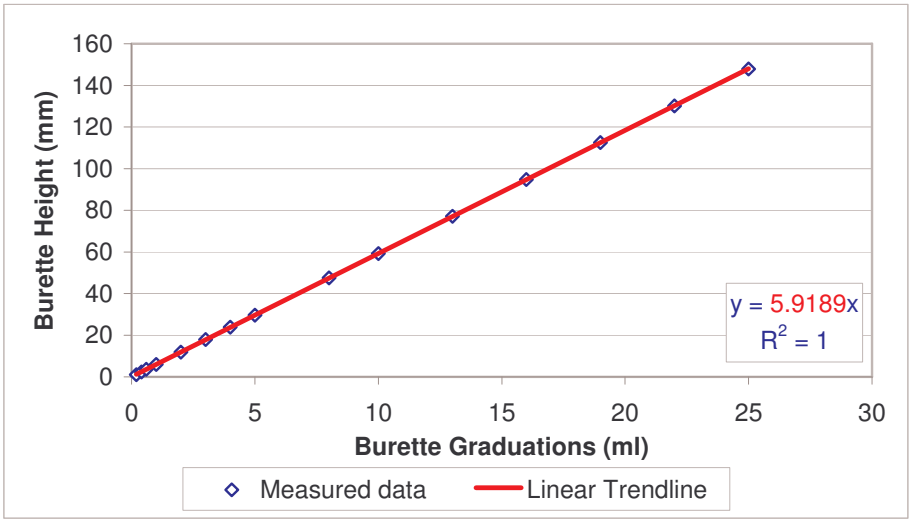

Figure 4.12 Details the linear conversion of burette graduations to the burette height.

6) Once each reading had been acquired a graph plotting actual pressure against the output signal from the transducer and the slope of the resultant linear trendline provided the calibration constant, as shown in Figure 4.13.

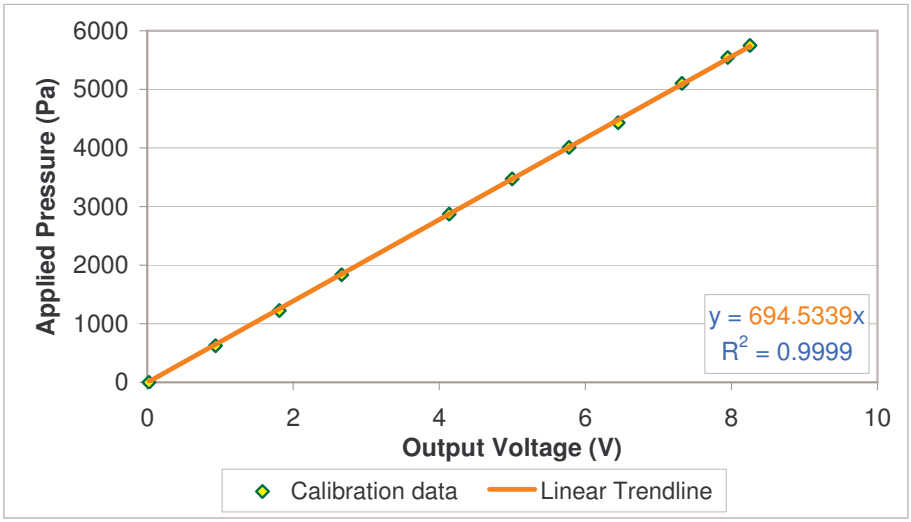

Figure 4.13 Shows the calibration results and the conversion constant.

After the calibration process had been completed it was discovered that the calibration data supplied with the Setra pressure transducer, provided a greater range of applied pressures which were accurate up to four decimal places. The results of the factory calibration test can be seen in Figure 4.14, as shown the calibration constant was slightly lower than the result obtained from the burette calibration. Consequently the factory calibration constant was used for all experiments as the accuracy of the calibration was clearly superior to the data obtained from the burette calibration.

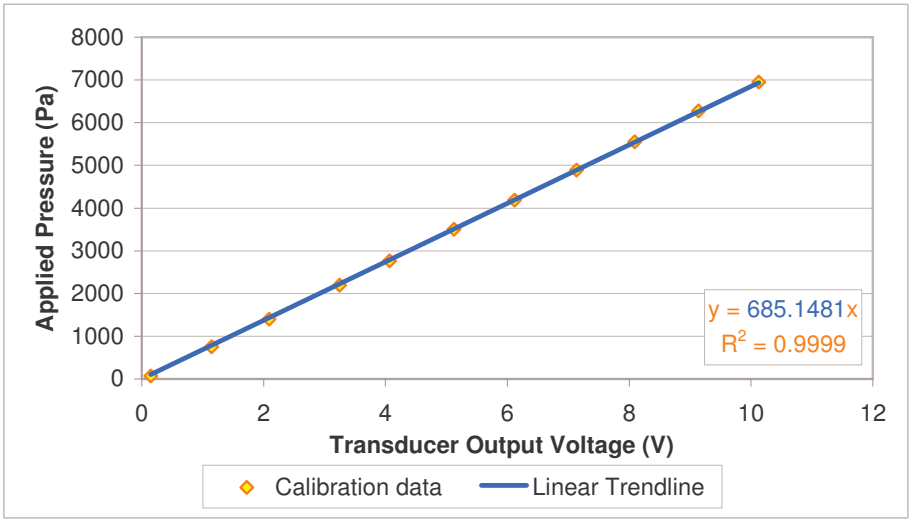

Figure 4.14 Details the factory calibration results and the conversion constant

4.7. Temperature Measurement

To provide a more accurate representation of the of the heat transfer process taking place in the microchannel samples it was decided and take eight individual temperature measurements rather than the six measurements used in the previous work (Eason, 2005). These measurements taken are as follows, microchannel surface, manifold surface and fluid temperature for both the inlet and outlet to the microchannel test sample and also the resistor surface temperature and reservoir fluid temperature. The surface temperatures of the manifolds were added to this experiment in order to account for any heat which may be transferred to the fluid from the inlet and outlet manifold surfaces. The microchannel surface and fluid temperatures at the inlet an outlet were required for the experimental and theoretical calculations and the reservoir fluid temperature was used as a rough estimate of the fluid temperature entering the microchannel test system. In the case of the resistor surface temperature this was simply used as a safety guideline to avoid overheating the system as the thermal epoxy used for mounting the resistors was only rated up to 120°C.

4.7.1. Thermocouples

The temperature measurements were achieved using two different types of K-type thermocouples. K-type thermocouples are made of two wires of dissimilar alloys Nickel-Chromium (Chromel) and Nickel-aluminium (Alumel), the point at which they are bonded together is temperature sensitive and generates a small voltage in response to a change in temperature. The K-type thermocouples were specifically chosen for these experiments because of there low thermal conductivity which ensures that the heat lost by conduction through the wires is kept to a minimum and therefore provides more accurate experimental results (Eason, 2005). For the temperature measurements taken inside the microchannel system Omega (model no. CHAL-005) bare wire thermocouples were used, which have a diameter of approximately 127μm (as shown in Figure 4.15) and therefore allowed thermocouple access to manifolds between the silicone gaskets. As the thermocouple wires were not insulated the double

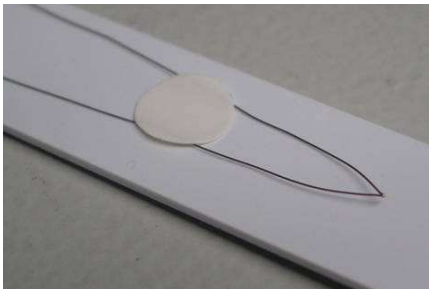

Figure 4.15 Shows the tip of an Omega bare wire thermocouple

layered silicone gasket provided a more than adequate seal around the bare thermocouple wire at the maximum flow rate supplied by the gear pump.

To monitor the reservoir fluid and resistor surface temperature standard Teflon insulated thermocouples made also of Chromel and Alumel materials were used. These thermocouples were much more robust and did not require the constant attention of the bare wire thermocouples to avoid contact with other metals to avoid altering the signal voltage.

4.7.2. Thermocouple Amplifier

In order to provide a stronger more robust signal from the thermocouples a signal amplifier was required. In this experiment a custom built thermocouple amplifier shown in Figure 4.16, capable of amplifying 12 thermocouple signals using Analog Devices AD595AQ chips, was used to implement the signal amplification. The AD595AQ chip, as shown in Figure 4.17 is equipped with cold junction compensation to account for the room temperature and has an accuracy of ± 3°C before calibration. The circuit had been previously built, however it required some modification to allow output signals of 0.01 volts per degree Celsius to be sent to the data acquisition software via a 25 pin connector, which offered straightforward integration of amplifier into the test rig.

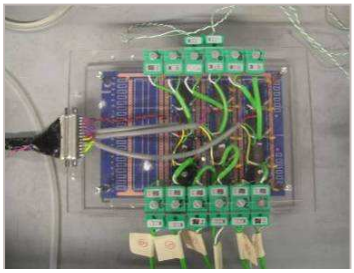

Figure 4.16 Details the thermocouple amplifier fully installed into the test rig.

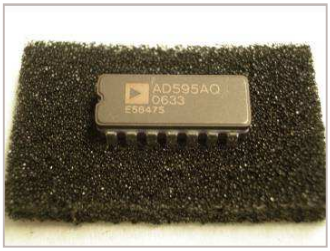

Figure 4.17 Shows an example of the 14 pin AD595AQ chip.

The thermocouples were connected to the amplifier using K-type connectors, as shown in Figure 4.16. In the case of the bare wire thermocouples where the positive (yellow) and negative (red) wires were fed into the aluminium manifold block from either side, it was necessary to remove the pins from the connector blocks to provide a more manageable set up. Insulated K-type extension leads were also used for each bare wire thermocouple to provide access to the amplifier and also

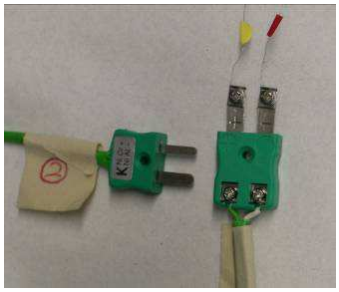

Figure 4.18 Details the connection pins and extension wire used with the bare wire thermocouples.

reduce the chances of the wires shorting of each other, details of the pin an extension wire can be seen in Figure 4.18.

Before commencing the experimental testing, the thermocouple amplifier circuit board was checked for loose connections. It was discovered that the Chromel and Alumel alloys of the thermocouple extension wires had not bonded adequately with the solder on the circuit and were therefore resoldered.

4.7.3. Thermocouple Mounting

To obtain an accurate representation of the temperature gradients inside the microchannel test system during the experiments it was extremely important that the bare wire thermocouples were mounted and positioned correctly. The following diagram Figure 4.19, shows the required position of the thermocouple beads for the microchannel surface temperature (1), the manifold surface temperature (2) an the fluid temperature (3) in both the inlet and outlet manifolds.

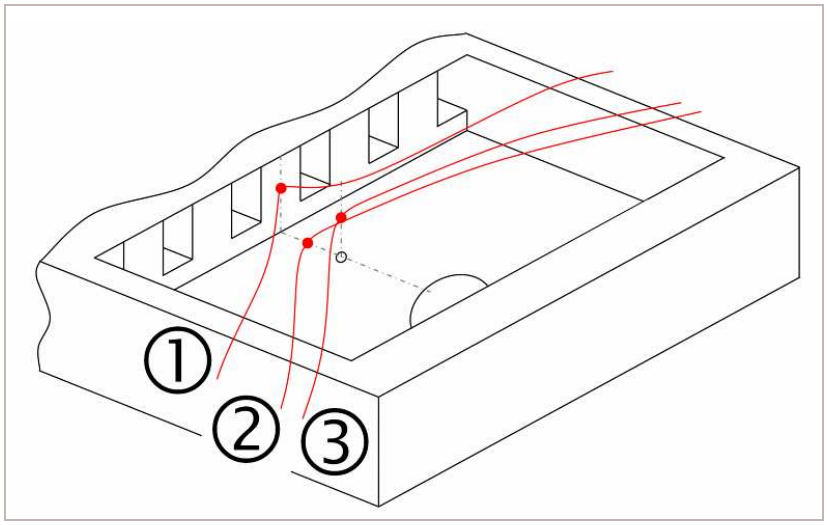

Figure 4.19 Illustrates the locations of the thermocouples inside the manifolds. (Eason *et al* 2007)

The microchannel surface thermocouple was the most complex of all the mounting procedures, the thermocouple bead was required to sit directly on the silicon surface of the wall separating the two central channels. This wall was approximately 400µm wide and therefore a 3D positioning stage was used to accurately align the thermocouple with the channel wall on the test sample. The positioning rig is shown in Figure 4.20. All thermocouples were mounted using Permabond 102 super glue which is a medium viscosity general adhesive with a service temperature range of -30 to +85°C. The following steps were taken to complete the mounting process.

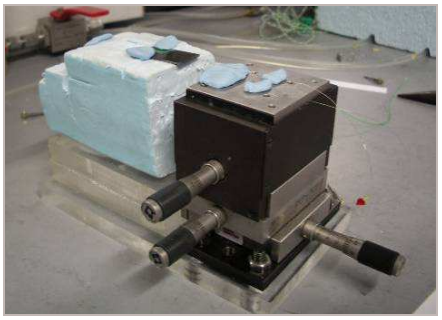

Figure 4.20 Shows the 3D positioning rig used for mounting micro channel surface thermocouples.

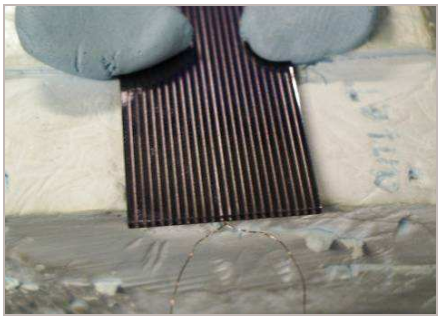

Figure 4.21 Shows the thermocouple mounted on the surface of the channel wall.

1) The microchannel sample was positioned on the polystyrene block along with the thermocouple on the 3D positional unit; both were held in placed with Blu-Tac.

2) At this point the thermocouple bead was aligned with the central channel wall using the 3D positioning unit.

3) Once positioned the thermocouple was moved back along the longitudinal axis of the microchannel sample to allow ample room to apply the adhesive.

4) A small amount of adhesive was applied to the thermocouple bead using some waste thermocouple wire and it was then quickly re-positioned on the surface of the channel wall (Figure 4.21).

5) Once the adhesive had dried more glue was applied around the thermocouple bead to provide a stronger bond with the silicon surface and also to insulate it, ensuring the channel surface temperature reading was not altered by the fluid temperature.

6) This last step (5) was repeated until the thermocouple appeared to have a secure bond with the channel wall; however it was important to allow the glue to dry between each application to avoid glue entering the microchannels.

7) When one thermocouple was mounted the test sample was carefully rotated and the previous steps were repeated to mount the second thermocouple.

If a microchannel became blocked with glue the thermocouples were removed and the test sample was placed in some acetone to soften the glue which was the removed used a small diameter wire.

In order to mount the thermocouples on the manifold surface in between the pressure tappings and the microchannel entrance or exit points, the thermocouples were first held in position using Blu-Tac, as detailed in Figure 4.22. In this case it was

imperative that the thermocouple bead was held in contact with the manifold surface, once this was achieved a small drop of adhesive could then be applied over the bead and allowed to dry. A mounted manifold surface thermocouple can be seen in Figure 4.23.

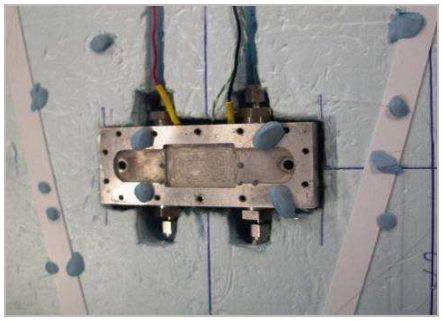

Figure 4.22 Details the mounting method used for the manifold surface thermocouples.

Figure 4.23 Shows the position of the thermocouple mounted on the manifold surface.

To mount the thermocouple on the surface of the resistors the surface was sanded down using some emery paper and mounted implementing the same process used earlier to mount the manifold surface thermocouple, the result of which is shown in Figure 4.24. The fluid temperature thermocouples were required to be situated directly above the pressure tappings at the inlet and outlet of the microchannel sample. This was simply achieved by holding thermocouple bead in place with blu-tac as the test system was sealed with the cover plate and the second gasket.

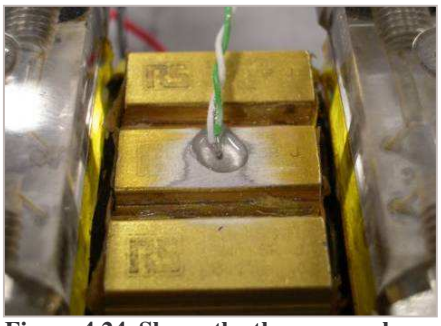

Figure 4.24 Shows the thermocouple mounted on the surface of the resistors.

To avoid shorting between different thermocouple wires and the manifold surface, a slight coating of adhesive was applied to the thermocouple wire exposed inside the inlet and outlet manifolds.

4.7.4. Thermocouple Calibration

To improve the accuracy of the temperature measurements the thermocouples and the thermocouple amplifier were calibrated using a Lauda RE 104 temperature controlled water bath which uses a PID controller and a platinum resistance thermometer to control the temperature the fluid (deionised water) in the bath.

In the previous work (Eason, 2005) the thermocouples were calibrated before mounting took place, however in this experiment, calibration took place with all the thermocouples mounted in there positions inside the microchannel test system. This calibration method was preferred as it accounted for the changes in the thermocouple resistance caused by accidental stretching and kinking of the wires during the experimental preparation and mounting. Any change in the resistance or strain levels of the thermocouple will produce a s change in the voltage signal generated and therefore render the calibration results inaccurate.

Figure 4.25 Shows the temperature controlled bath and the set up used during calibration.

The calibration process was completed as follows

1) Firstly the upper edges of the stainless steel water bath and any metallic surfaces on the microchannel test system were covered with insulating tape to avoid shorting the bare wire thermocouples.

2) The microchannel test system including the thermocouples mounted in the correct positions was overturned and placed into the water bath along with the reservoir thermocouple.

3) The correct wires for each thermocouple were then paired and fixed to the edge of the water bath with insulating tape. Each wire was placed under tension to ensure the wires did not touch off each other or the surface of the bath under the water level, when the water bath was turned on.

4) Each thermocouple was the assigned a channel in the thermocouple amplifier which remained fixed for the duration of the experiments. Extension wires used for the six bare wire thermocouples also remained fixed for the experiments. This guaranteed the accuracy of the calibration data for each temperature measurement.

5) At this stage the set point of the temperature controlled water bath was set to a temperature lower than lowest temperature expected from testing. In this case 18°C was used as it is much lower than the room temperature of the laboratory.

6) The temperature controlled bath was then switched on, and allowed to reach a steady state. At this point the temperature readings from each thermocouple were recorded through the LabVIEW control program for approximately thirty seconds.

7) The set point of the bath was then increased in stages up to 78-80°C (which was higher than the maximum temperature expected during testing) and the temperatures were recorded as described in (6) for each stage.

The following graphs (Figure 4.26 & Figure 4.27) show the deviation in the temperature readings from temperature of the water bath, for the eight thermocouples used on the DRIE and wet etched microchannel samples.

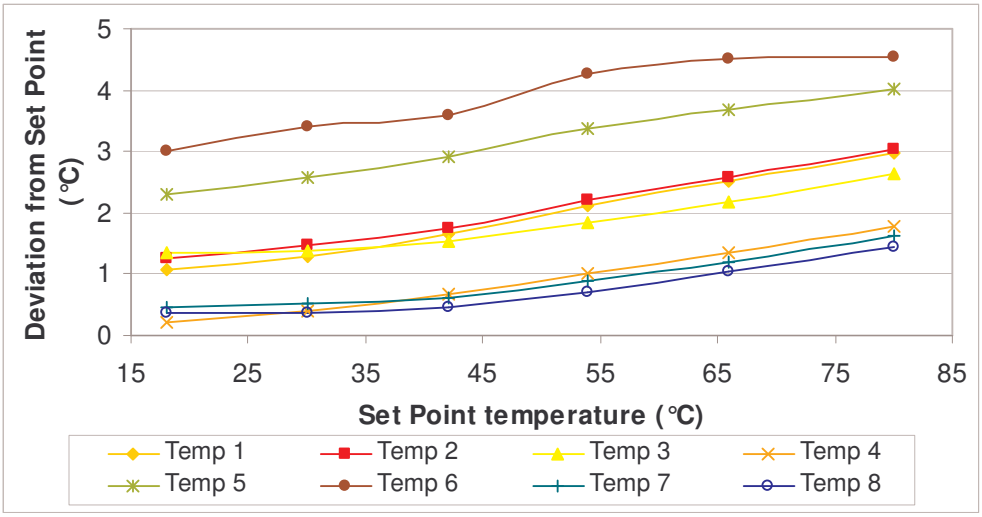

Figure 4.26 Details the devation in thermocouple temperature readings from the water bath set point for the DRIE channels.

It was initially planned to calibrate the thermocouples before testing but after the first tests were performed on the DRIE channels a second calibration test was completed and it was discovered that the calibration data had changed (again from stretching and kinking) from the previous test. Therefore the calibration was completed after testing for the rest of the experiments on heat transfer.

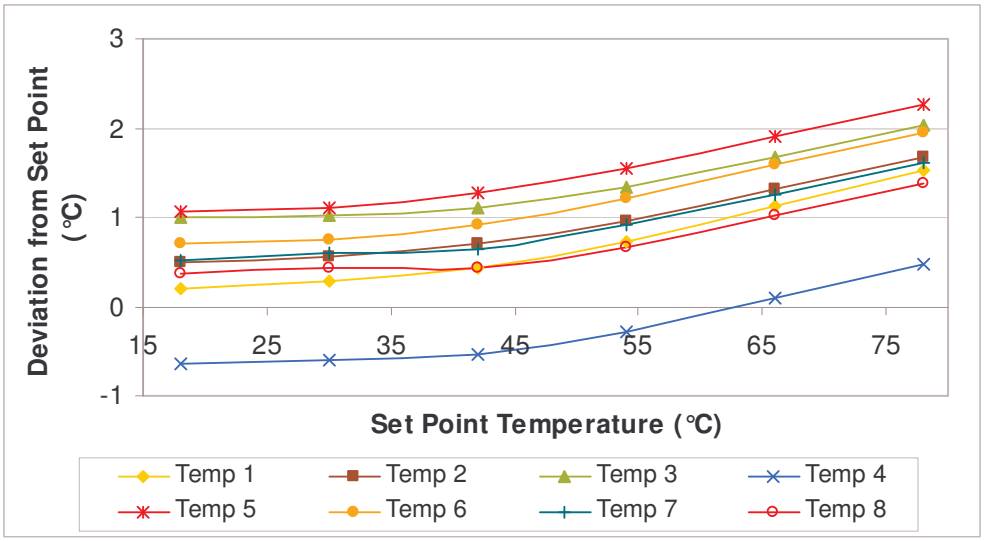

Figure 4.27 Details the deviation in the thermocouple temperature readings from the water bath temperature for the wet etched sample

In order to implement this calibration data, a MATLAB program written for the previous work (Eason, 2005) linearly interpolates between the calibration set point temperatures to discover the actual temperatures being observed by the indicated experimental temperature readings. This program is used to convert all the experimental temperature measurements into their corresponding actual temperature values and thus allowing the properties of the system to be accurately calculated.

4.8. Data Acquisition

The previous work (Eason, 2005) the mass flow rate was measured manually and the pressure drop measurements were collected by recording the display reading from a voltmeter. This data was then compiled along with the logged temperature data for analysis, in this experiment the data acquisition process was to be automated. In order to provide a means of continuously displaying and rerecording multiple streams of experimental data, the National Instruments LabVIEW (Laboratory Virtual Instrumentation Engineering Workbench) software was used. LabVIEW is a general purpose programming software, which uses a graphical based programming language (G) to create programs in a block diagram form. The software contains extensive libraries of function blocks which can be used for any programming task. Each function block contains the necessary code to carry out its purpose and can be joined together to provide data acquisition, instrument control and also process automation.

For these experiments the LabVIEW software was required to fulfil the following tasks.

1) Provide an output signal to control speed of the pump motor.
2) Read in the mass flow meter signal incorporating the conversion constant to show the actual mass flow rate on screen.
3) Read in the output signal from the pressure transducer and using the conversion constant and a zero offset, present the pressure drop across the microchannel test sample on screen.
4) Allow the required data to be logged directly into a Microsoft Excel file (.xls). This also required file path designation and on screen File naming and On & Off switching.
5) The program required a means of changing the rate of sampling, where the time between readings could be altered on screen.
6) In the case of the heat transfer measurements the temperature signals needed to be read in and converted the degrees Celsius to display the individual temperatures on screen.

In order to interface the PC and the LabVIEW software with the individual devices used in the test rig, a National instruments PCI-6251 card coupled with the SCB-68 connector block was used. This system can accommodate 16 Analogue inputs, 2 Analogue outputs and 24 digital inputs or outputs with 16 bit accuracy at 1 million samples per second for multi-channel use (National Instruments, 2007). The SCB-68 connector block provides easy to use screw terminals for output or input signals. Both the PCI-6251 and the SCB-68 are shown below in Figure 4.28.

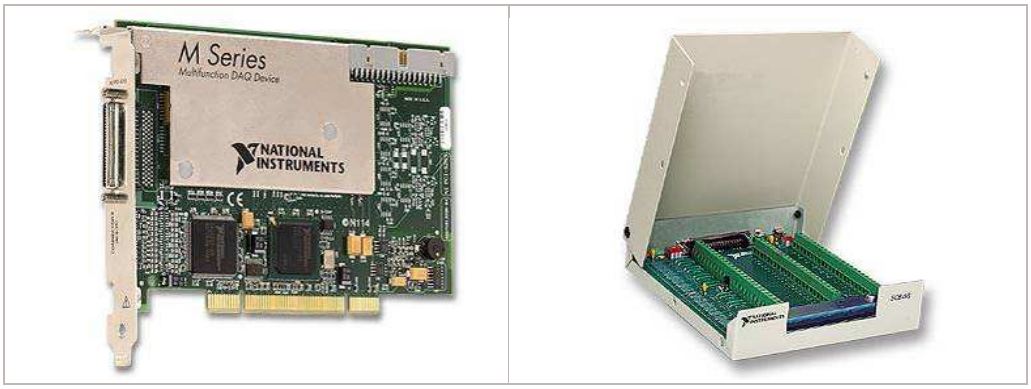

Figure 4.28 Shows the National Instruments PCI-6251 card (left) **and the SCB-68** (right) **connector block** (National Instruments, 2007).

The programming for LabVIEW took place continuously throughout the work on this project with small programs being developed for each calibration process, however there were two main programs were created, one for the pressure drop experiments and another for the heat transfer experiments.

In the case of the pressure drop experiments, the program was required to record only the time between measurements, the mass flow rate and the pressure drop across the channels. The temperature of the reservoir was taken using a hand held thermocouple reader (Kane-May KM330) and therefore reduced the need for thermocouple calibration. The block diagram and front panel display used for the pressure drop experiment program is shown in Figure 4.29 (Please note that all programs images are displayed in more detail, in *section B* of the appendices). It is important to note that both images in Figure 4.29 are linked and all items that appear on the front panel display are labelled in the block diagram with in a black border and a white background. As detailed in the block diagram the majority of the components are contained within a grey box, known as a *While Loop*. The While loop is governed by the time between the measurements and for actual experiments this was set to 0.25. Therefore any component held inside this loop was run 4 times a second once the program had started and continued to run iterations until it was stopped.

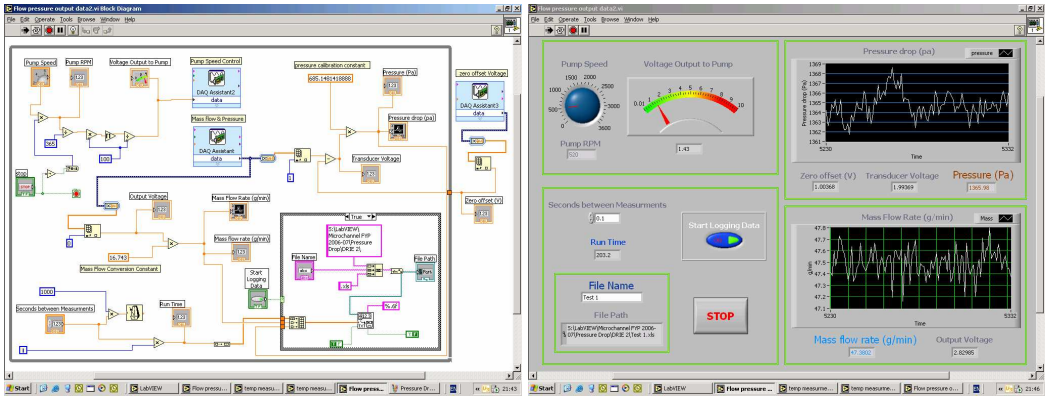

Figure 4.29 Shows the Block Diagram (left) **and the Front Panel Display** (right) **of the LabVIEW program used for the pressure drop experiments.**

The pressure drop program completed five of the six required tasks (1-5, previous page) for the data acquisition using LabVIEW. In the case of the pump speed control (top left corner in both images) the required pump rpm could be chosen on the front panel. In the block diagram, this signal was sent to multiplier block where it was multiplied by one when the program was running and zero when it had stopped. This

ensured the pump did not continue to run once the program was switched off. The pump speed signal then continued on to be multiplied by the conversion constant, after which the resultant signal was rounded off to an even number in the next three blocks. This correction was necessary as the pump motor could not process signals to the same resolution as the PC and therefore the signal had to be exact to ensure the pump speed would change by increment of 10rpm. The rounded signal was then sent to a display on the front panel and also to a *DAQ Assistant* where the signal was sent to the pump motor. The DAQ Assistant allows the user select conditions for input and output signals, for example assign signals to specific channels in the connector block and adjust the signal limits ±5V or ±10V.

As previously stated the DAQ assistant also controls the input signals, a single DAQ assistant can read in as many signals as the PCI card can provide. However, to read in multiple signals you have to assign a scan order which is a ranking scale with zero being the first signal to be scanned. As shown in Figure 4.29, the mass flow rate and pressure transducer are assigned a scan order of 0 and 1 respectively. Firstly looking at the mass flow rate system (centre of block diagram) the signal was converted and sent through an index array with the correct scan order applied to it (blue numeric box). The index array sorts only the mass flow rate data into a 32bit signal or double signal. This signal was then multiplied by the conversion constant (volts to g/min) and sent to a waveform graph and numeric box which displayed the mass flow rate on the front panel (top right corner). The Pressure transducer signal was converted using the same process as the mass flow rate, although before the conversion constant was multiplied in, the initial pressure transducer signal (the zero offset) was subtracted from the incoming signal and thus zeroed the signal. The zero offset voltage was measured using the DAQ assistant outside the while loop which runs a single iteration before the while loop starts, to measure the pressure transducer voltage when no load is applied.

To provide a method of switching on and off the data logger, the cluster of function blocks was placed into a *Case Structure*. A case structure consists of two sections a true and a false section, which are selected via a switch but cannot run simultaneously. In this program, when the switch is on the true section containing the logging functions will run and when it is off the false section which is empty will run and therefore providing on and off control of the data logger. The data logger system

simply used the 'Write a text file' function to save the required logged data which was received via the build array block which organises this data into an array of columns. Subsequently, the file path (file destination on the harddrive, set in the block diagram) the file name and the file format (.xls) (both set from front panel) had to be specified. This data (located in the pink boxes) was compounded together and sent to the write to txt file function where an Excel file of data columns in the order of which they were inputted was created and saved according to the selected file parameters.

To control the sampling time of the program the seconds between measurements inputted was adjusted on the front panel and on the block diagram (bottom left corner). The signal was multiplied by a thousand and sent to a delay function, which operates in milliseconds. This function then delays the next iteration of the while loop by the required duration. In order to calculate the running time of each program run, the value from the seconds between measurements input was multiplied by the number of iterations completed by the while loop. This signal was also sent to the data logger and provided a time line for the data being recorded.

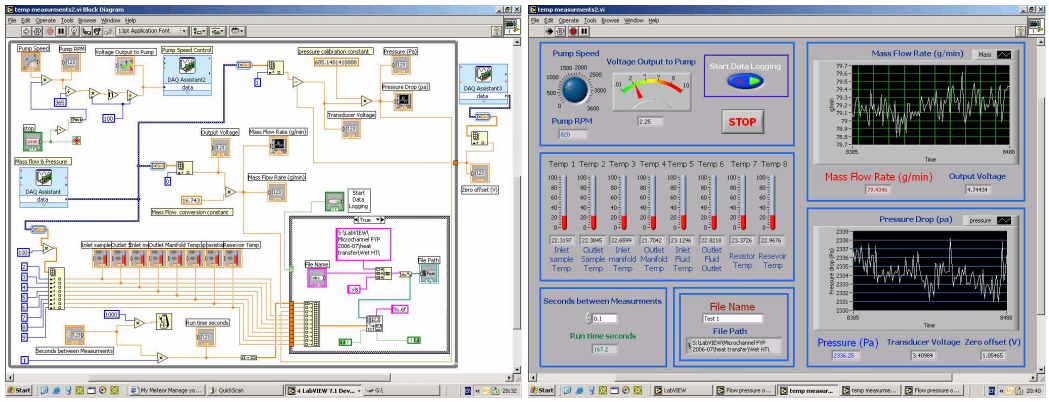

Figure 4.30 Displays the Block Diagram (left) **and the Front Panel Display** (right) **of the LabVIEW program used for the heat transfer experiments**

Essentially, the program developed for the heat transfer experiments worked off the same principle of operation used in the pressure drop program. This program completed all of the required tasks for data acquisition as stated earlier and details of the block diagram and front panel display are shown in Figure 4.30. This program was required to log the run time, mass flow rate, pressure drop and all eight temperature measurements. These temperature measurements were allocated an individual channel in the connector block and also assigned a scan order number in the block diagram. A

voltage signal of 0.01V from the thermocouple amplifier corresponded to a temperature of 1°C and therefore all temperature signals were multiplied by 100 to represent the signal in degrees Celsius. From here, the individual temperature signals were split up using the scan order and displayed on the front panel as shown in Figure 4.30. These individual temperature signals were then passed on to the data logger and saved in an excel file along with the previous data mentioned earlier.

4.9. Microchannel Area Measurement

As the dimensions for all channels are created on a micro-scale it was important that the cross sectional area (CSA) of each channel was measured. This ensured that small changes in the manufacturing process, which could produce large changes to the CSA of each of the channels was accounted for and therefore provided more accurate experimental results. The area was calculated by taking scaled measurements from digital microscope images of each channel, using the apparatus shown in Figure 4.31.

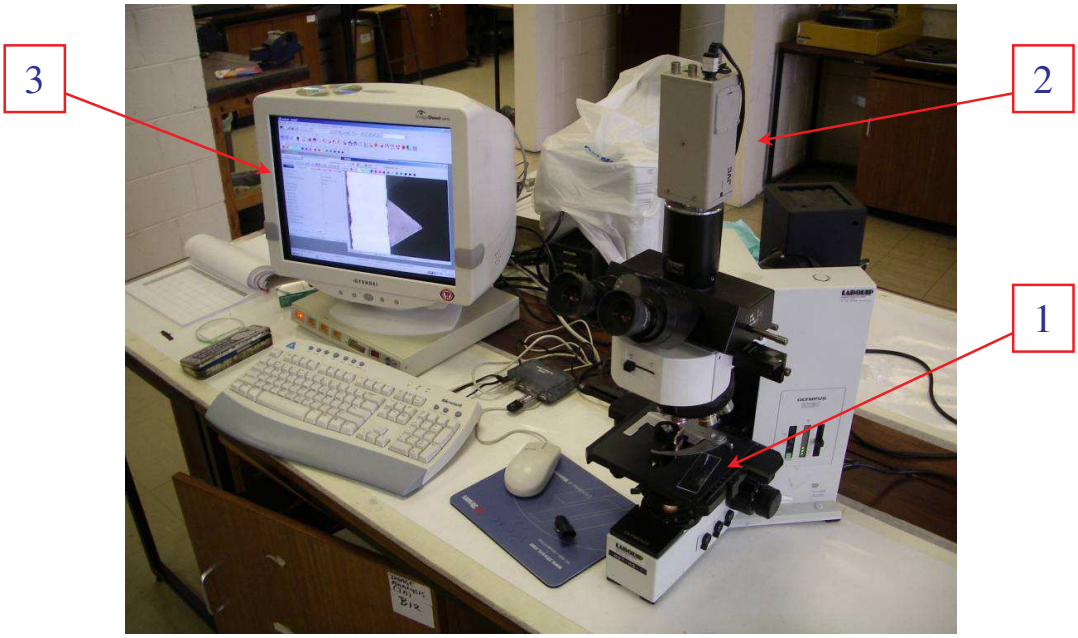

Figure 4.31 Shows the Microscope (1), CCD camera (2) and PC (3) set up used to photograph each microchannel cross section.

In order to calculate each CSA of each the following steps were completed:

1) First the length of each test sample was measured. After which the edges of the sample's surface was placed on a sanding wheel to provide a cleared outline to each channel cross section.

2) The samples were then placed under the microscope (Olympus BX60) with the light shining up from underneath, as shown in Figure 4.32. Photographs of each individual channel on both samples were taken using a JVC CCD camera which relays the images to a PC.

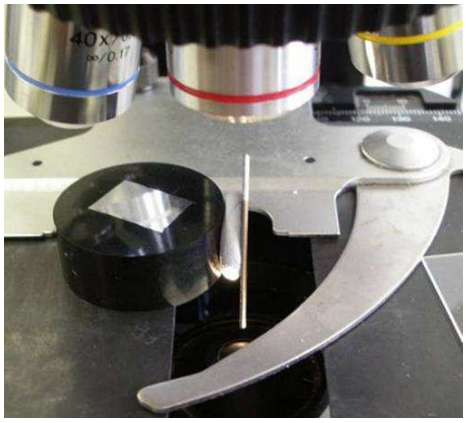

Figure 4.32 Shows the microchannel test sample held under the microscope lens.

3) In order to scale these images taken, pictures of a precision slide with graduations of 1 micron, placed in both the vertical and horizontal directions were also taken.

4) From here these images were brought to Jasc Paint Shop Pro program where a new layer was applied to the image. Three single pixel red dots were placed on this layer to mark the upper left and right Green dots were then placed in the middle of the graduation lines furthest apart and the distance is noted.

5) Once the dots have been positioned the background image is hidden and the file is saved as a gif file (only 256 colours)

6) In the case of the microchannels it was decided to measure 5 or 6 channels on each sample fully by placing green dots all around the channel outline. The rest of the channels were measured using four points to create a height and a width, which accurately represented the area of the channel being measured. This method was used for both channels shapes (as shown in Appendix C).

7) All channel images were then saved as gif files as stated in (5) and each image was scanned using a MATLAB program developed in the previous work (Eason, 2005). This program scans the image from left to right recording the position of the green dots and scales each point according to the distance measured in step (4).

8) The MATLAB program produces a text file of the individual channels with the x, y and z (equal to zero) co-ordinates for each scanned green pixels. As the program scans the image from left to right these points must then be sorted into the proper order in Excel, as shown in Figure 4.33.

9) The sorted points for the fully mapped channels are then imported into ProEngineer (CAD program) where a spline line was plotted through each point. The spline line was then joined to the first point to complete the shape of the cross section and thus allowing the shape to be extruded, as shown in Figure 4.34.

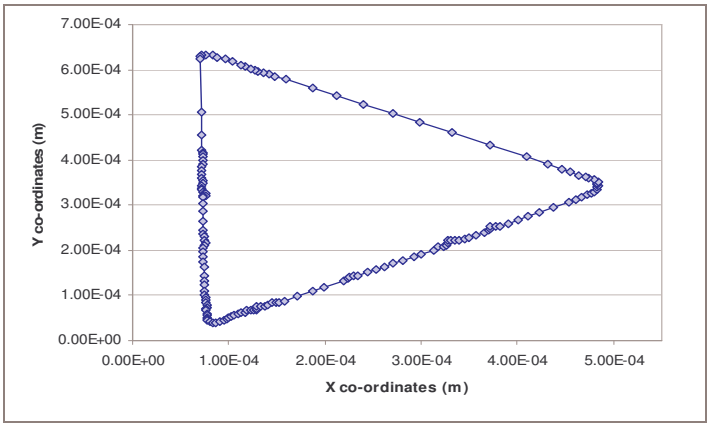

Figure 4.33 Shows the graph of sorted outline points in Excel

10) At this point the measure function in ProEngineer was used to calculate the CSA of the channel for each completely mapped channel. The results of the height and width measurements are then multiplied out to calculate the remaining channel CSA's.

11) At this point the CSA's for each test sample were averaged to develop a standard CSA to be used in the experimental and theoretical calculations.

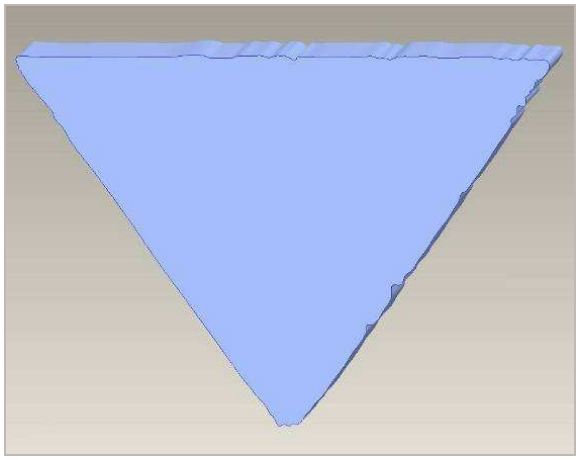

Figure 4.34 Shows the extruded cross section of the measured channel in ProEngineer.

More details on the microchannel area measurement are contained in the *Appendix C*. In this section the microscope images and the outlining methods for the different types of channels are shown along with the gif files for each solution. The source code for the MATLAB program used for scaling the individual points can be found on the attached CD at the back of this report.

5.0 Experimental Procedure

In this section the practical experimental procedure used to perform the pressure drop and heat transfer experiments on the two sets of microchannel samples is outlined.

5.1. Pressure Drop Experiments

For these experiments the data required was the Run Time, the Mass Flow Rate, the Pressure Drop across the channels and the average temperature of the working fluid. As the thermocouple calibration process was quite time consuming, it was decided to use a hand held thermocouple reader (Kane-May KM330) with a 0.1°C accuracy to measure the temperature of the working fluid inside to reservoir. This temperature was required to calculate the correct fluid properties of the system during the experiment and was simply recorded at the end of each test run and added to the Excel file that was generated. The following steps were performed to complete this experimental pressure drop test:

1) Firstly the system was set up as shown in Figure 4.1 with a microchannel sample held in test system. It should be noted that the thermocouples and amplifier were omitted from the experimental test rig during these experiments.

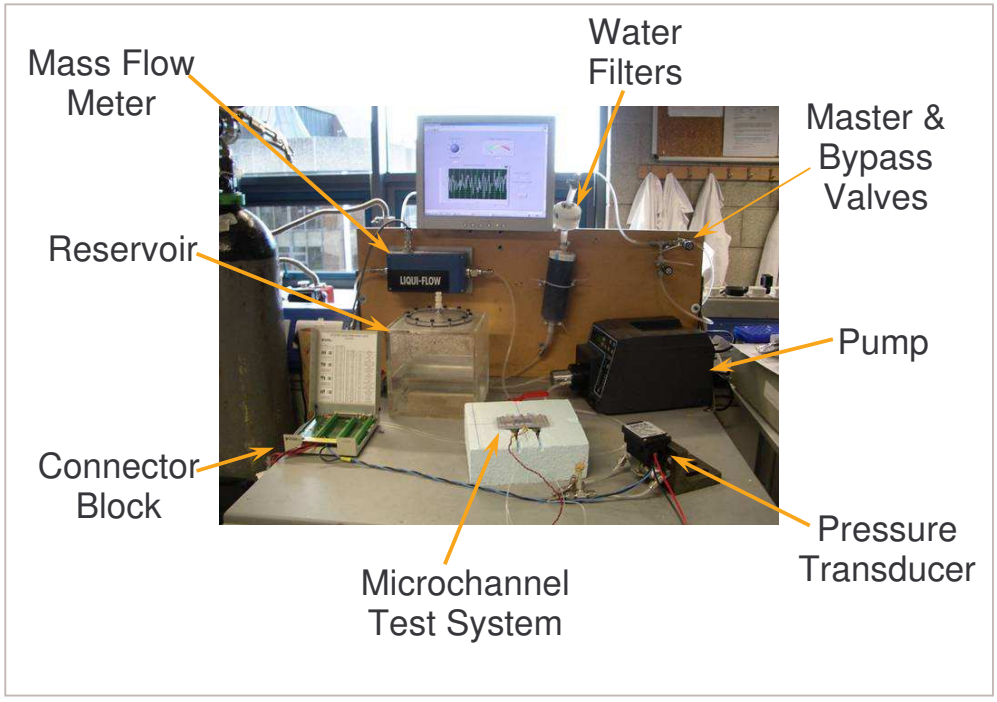

Figure 5.1 Details the test rig layout used during the pressure drop experiments.
(note the pressure transducer was later moved to a separate table to eliminate the noise vibration from the pump)

2) Any air bubbles were removed from the system and the pressure transducer was bled as previously described in section 4.6.

3) Once the set up had been completed the maximum operation conditions of the system were established. In the case of the DRIE channels this was limited by the pressure transducer which reached its maximum reading at mass flow rate approximately 110g/min. For the wet etch samples this limit was governed by the mass flow meter which could only measure up to 177g/min.

4) Ten evenly spaced points between the lowest operating condition (60rpm pump speed) and a point slightly below the maximum limit of operation were then decided upon, to provide adequate sampling across the operating range of the test rig in each case. For these experiments the pump speed was used to govern the point for each experimental reading

5) Once the testing points had been decided, a thermocouple was placed into the reservoir and connected to the hand held monitor as shown in Figure 5.2.

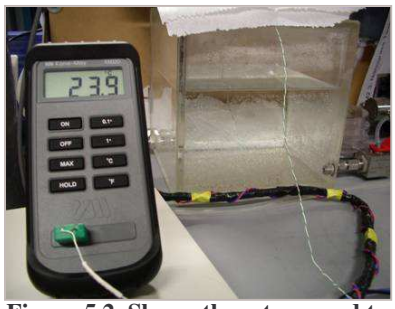

Figure 5.2 Shows the set up used to record the reservoir fluid temperature.

6) At this stage the LabVIEW control program was opened and the first experiment was performed. This was achieved by setting the pump speed to the required output, allowing the system to reach a steady state which took approximately 10-15mins

7) Once the system had reached a steady state the file name was assigned and the data was logged at 4 samples for a period of one minute. During the data logging period the temperature of the reservoir fluid was monitored and an average temperature was recorded in the resultant Excel file.

8) The pump speed was then set to the next experimental point and during the time spent waiting for steady state conditions, the validity of the data from the previous test was checked. This involved plotting the collected data and checking if the system had reached a steady state (slope of curve equal to zero) and also examining the results for the presence of unwanted any disturbances. If any

problems were found the previous test was repeated until the data recorded was suitable for theoretical analysis.

9) Steps (6, 7 & 8) were then repeated for all the other experimental points and the result of the testing produced Excel files containing the experimental pressure drop, mass flow rate and average fluid temperature for each of the twelve experimental points.

10) All steps from (1) to (9) were then repeated to acquire experimental data for the other microchannel test sample.

During and close to the data logging periods it was imperative that the test rig was not disturbed as small bumps and movements could be sensed by the testing equipment and therefore produce inaccurate experimental data. For this reason it was vital that after each test the data was inspected for the presence of any disturbance.

5.2. Pressure Drop and Heat Transfer Experiments

In these experiments the logged data was as follows,

- Run time - (s)
- Mass Flow Rate, $\dot{m}$ - (g/min)
- Pressure Drop, P_{Lexp} - (Pa)
- Inlet and Outlet Test Sample Surface Temperature, T_{inS} , T_{outS} - (°C)
- Inlet and Outlet Manifold Surface Temperature, T_{inM} , T_{inM} - (°C)
- Inlet and Outlet Fluid Temperature, T_{inF} , T_{inF} - (°C)
- Resistor Surface Temperature, T_{RS} - (°C)
- Reservoir Fluid Temperature, T_{RF} - (°C)
- Power input to the resistors Q - (W) recorded manually

The system layout used for these experiments is shown in Figure 4.1, for this layout an additional power source was also required to provide power to the heating resistors. In these experiments five points were equally spread across the operating range between the maximum and minimum limit points of the system, thus providing seven experimental operating points. At each experimental point the heating resistors were subjected to a Low, Medium and High power supply. These power supplies were selected at each experimental operating point by specifying the Low power setting (a change between inlet and outlet of at least 2°C) followed by the High power

setting (below Resistor surface temperature of 120°C) and then picking a power setting between these two settings for the Medium power supply. The power supply readings were recorded manually by taking the product of the voltage and current output of the power source. The following steps were performed to complete the Pressure Drop and Heat Transfer experiments.

1) Once the system had been set up with all the thermocouples in place the reservoir opening valves were closed and a vacuum pump was attached to the lid of the reservoir and run for a couple of minutes. This vacuum pump sucks any gases out of the water and reduces the development of bubbles in the manifolds of the test system when heat is applied by the resistors.

2) After degassing the water there was quite a lot of air bubbles present in the tubing of the test rig and therefore the pump was run at full seed for a short period and the pressure transducer was bled according to section 4.6.

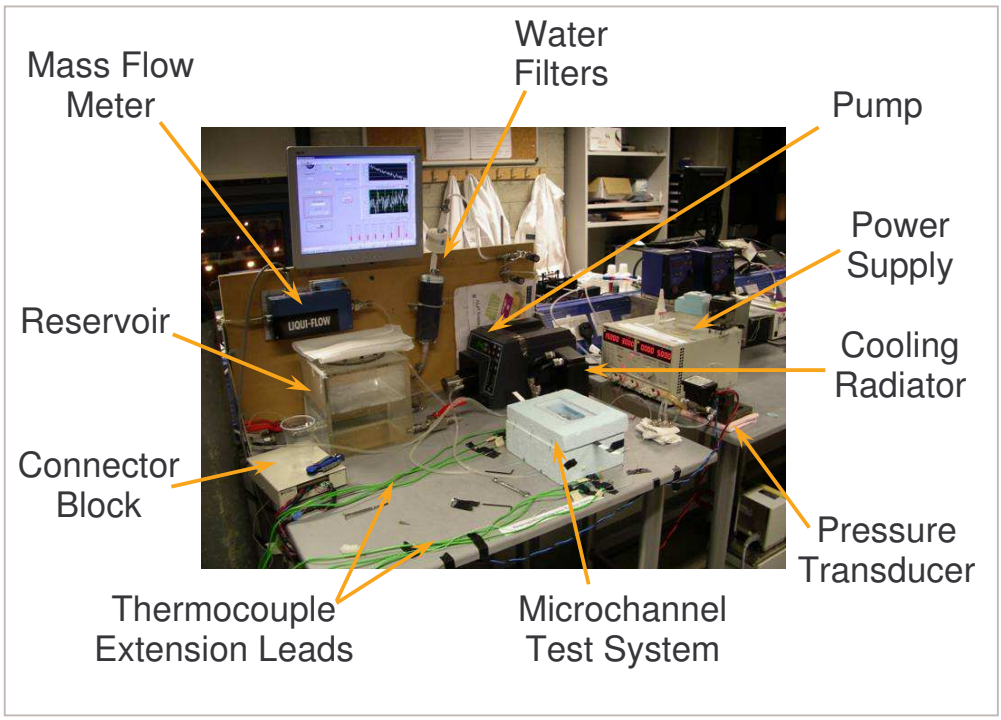

Figure 5.3 Shows the test rig layout used for the Pressure Drop and Heat Transfer experiments.

3) At this stage the system was laid out as shown in Figure 5.3. The LabVIEW program was then opened, the file destination was assigned and the seconds between measurements was set to 0.25 seconds.

4) The pump speed was then set to the required output along with a low power supply to the heater resistors (providing a change of at least 2°C across the channels) and the system was allowed to reach a steady state which took about 10-15mins.

5) Once the system reached a steady state the file name was assigned and the data logger was switched on. As there were lots of different signals being logged it was decided to log the information for a long period as this ensured there would be ample steady state data for the experimental analysis.

6) Once the data had been logged the system was left operating at the present conditions while the validity of the data was investigated. By graphing the results the data could be checked for the presence of any disturbances and if steady state conditions had been reached during the test. With the system still set at the same conditions, another set of data could then be taken under if required and thus avoiding the need to wait for steady state conditions on the second run.

7) When the recorded data set was deemed suitable for experimental analysis the product of the power supply output voltage and output current was recorded manually and then added to the Excel data file.

8) After the testing, the inlet and outlet manifolds were checked for the presence of air bubbles. If air bubble were present the cross over valve to the transducer was opened and the pump speed was increased to its maximum until the bubbles were evacuated. If air bubbles remained trapped between thermocouple wires the test system was tapped gently with a spanner and tilted to help release the air bubbles.

9) When the manifolds were clear, the pump was turned off and once the mass flow rate had reached zero the cross over valve was closed and the LabVIEW program was stopped. The program was then restarted, which allowed the pressure transducer zero offset to be recalculated and thus providing a more accurate pressure reading. Once the program was restarted the pump speed was returned to its previous value and the system was allowed to stabilise.

10) The power to the resistors was increased to the high power setting which was found using trial and error, to discover a setting which kept the surface of the resistors temperature below 120°C at the current mass flow rate. The steps (5 to 9) were then repeated for this setting.

11) Once the high power testing was completed a medium setting was established by using a power setting which produced temperatures approximately half way between the temperatures recorded for the previous Low and High settings. The steps (5 to 8) were then repeated to acquire data for that setting.

12) At this stage the low, medium and high power testing had been completed and experimental data was recorded for each case. Step (9) was then repeated, however the pump speed was changed to the next experimental operating point and a low power setting was applied to the heating resistors.

13) The system was then allowed to stabilise and steps (4) to (12) were repeated for the rest of the experimental points.

14) Once the testing was completed the thermocouples were calibrated and the next microchannel test sample was prepared for testing where the whole process was repeated again.

Again it was extremely important to avoid contact with the test rig when data logging as the pressure transducer was very sensitive and any bumps or movements were clearly recorded in the logged data stream. During testing it was essential to regularly check the thermocouples to see if any bare wires had come in contact with each other or any other metal and also to make sure the microchannel test system was covered with the polystyrene lid at all times to insulate the system.

6.0 Result Processing

In this section the methods used to process the experimental data acquired from testing are described. This section also details the programs used to generate the experimental and theoretical results along with their upper and lower uncertainties.

6.1. Experimental Data Processing

As a result of the experimental tests there was a considerable amount of logged data collected for each system setting. In order to calculate accurate experimental and theoretical results each data set was analysed to establish the points at which the experimental test rig had reached steady state operation and also when logged readings appeared to have the least amount of disturbance. As previously stated all the experimental data was logged at four times a second and it was decided to use a limit of 50 samples for the experimental and theoretical analysis. Figure 6.1 shows the logged data from the pressure drop and heat transfer experiments on a Wet etched test sample.

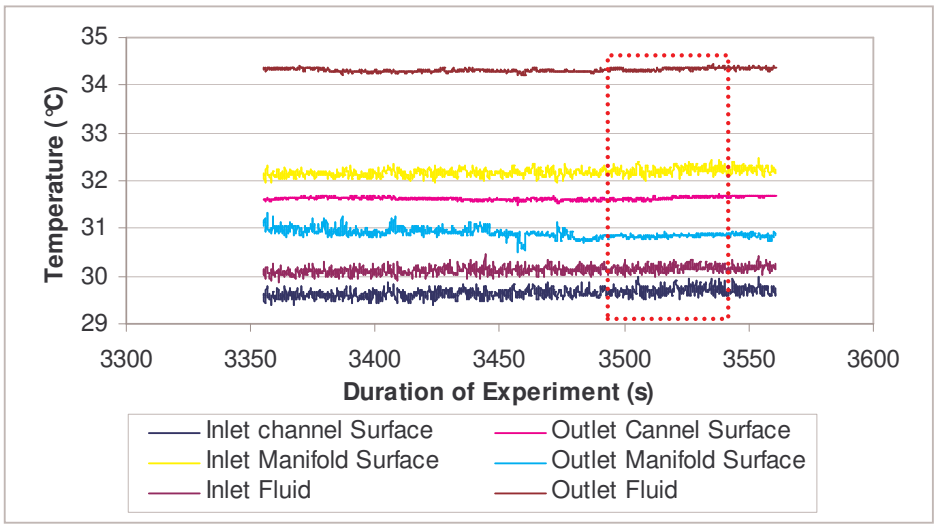

Figure 6.1 Shows the 50 samples which were taken for analysis from this data set.

The readings enclosed in the red box, shown in Figure 6.1 were the 50 samples used for the experimental analysis. This sample region was chosen because it was the area which appears to at a steady state and also the noise disturbance was at a minimum through this area. It should be noted that only these six readings are shown for clarity as the pressure drop in Pascals is much greater than these values. The calibration data for these thermocouples has not been implemented and therefore the outlet manifold

surface (Temp 4 in Figure 4.27) appears lower than the inlet manifold surface (Temp 3 in Figure 4.27).

The 50 samples were then averaged to one data point thus reducing the effect of noise in the experimental readings. The resultant points for each data set were then processed using MATLAB programs written for the previous work (Eason, 2005). These programs analyse each data point individually and calculate the properties of each point to establish a theoretical value to correspond to the average experimental data.

The uncertainty for each average point was calculated by taking the standard deviation across the 50 samples and multiplying the result by 1.96 to give a symmetrical 95% confidence interval (CI). This method provides a much more conservative estimate of the measurement of uncertainty as it provided a value which was higher than both the published manufacturers and the calibration uncertainty (Eason *et al* 2007).

6.2. Area Compensation

As the channels used in this experiment were not perfectly rectangular and trapezoidal shapes due to slight discrepancies in the manufacturing process. The theoretical correlations used to produce friction factors (*f*) for perfect shapes would not accurately predict the actual pressure drop across the channels (Eason, 2005). To provide a means of compensating for the deviations in channel shape, more detailed measurements of the channel cross section than just single width and height measurements was required. The process used to measure a more accurate CSA was described previously in section 4.9.

The pressure drop across the channels was calculated using Darcy's equation (Eqn. 7), which assumes the channels to be perfectly rectangular or trapezoidal and therefore requires compensation. As the experiments all take place with laminar flow passing through the channels, it is safe to assume that *fRe* is a constant as shown below.

$$fRe = c \qquad \therefore\ f \approx \frac{1}{Re} \qquad \textit{(Eqn. 19)}$$

By substituting the equation with the individual components of *Re* into Darcy's equation (Eqn. 7) gives the following

$$P_L \approx \frac{\mu L u}{D_h^2} \qquad \textit{(Eqn. 20)}$$

Assuming the following relationships of D_h and u to the area (A), Darcy's equation can be further simplified to Equation 23.

$$D_h^2 \approx A \quad \text{and} \quad u \approx \frac{1}{A} \qquad \textit{(Eqn. 21 \& 22)}$$

$$P_L \approx \frac{1}{A^2} \qquad \textit{(Eqn. 23)}$$

Equation 23 can then be modified to derive a compensated pressure drop *(Eqn. 24)* based on the original pressure and the ratio between the average of the CSA (A_{Exact}) for six channels measured using ProEngineer and the corresponding CSA (A_{Theory}) calculated by assuming a perfect shape. All area compensated pressure results are represented by *acomp* in the results section.

$$P_{L_{Comp}} = \frac{P_{L_{Theory}}}{\left(A_{Exact} / A_{Theory}\right)^2} \qquad \textit{(Eqn. 24)}$$

6.3. Temperature Normalisation & Compensation

During the heat transfer experiments the fluid temperature inside the microchannel test system varies across the test samples. Therefore to provide an accurate representation of the fluid properties at each experimental data point, an average of the inlet and outlet temperatures was taken and used to define the properties of the fluid within the system. This process is known as normalising and was calculated using the *water_prop.m* program written for MATLAB (Eason, 2005). This program linearly interpolates between water property data which is stored in a text file to calculate the density (ρ), viscosity (μ), thermal conductivity (k), specific heat capacity (c_p), latent heat of vaporisation (h_{fg}) and the Prandtl number (Pr) for the average temperature of each data point.

Once the temperature normalisation has been completed it can also be beneficial to converge these data points at a single temperature, as this provides more meaningful result plots with experimental data falling along the same line as the theoretical data for a common temperature. This temperature compensation was applied to the experimental and theoretical results by multiplying each result by the ratio of each of the component fluid properties at the experimental temperature (T_e) against the target

temperature (T_T). The mass flow rate data is unaffected by temperature changes and therefore does not require temperature normalisation or compensation, however the pressure drop across the channel as an example of the application of temperature compensation at 20°C is shown in Equation (25).

$$P_{L_{T20}} = P_{L_E}\left(\frac{\mu_{T_{20}}}{\mu_E}\right)\left(\frac{\rho_E}{\rho_{T_{20}}}\right) \qquad \textit{(Eqn. 25)}$$

6.4. Manifold Heating Effect

As shown in section 4.3.1 the heat power resistors apply heat to the microchannels through the aluminium block and therefore some heat is dissipated along the aluminium block and transferred to the fluid from the surface manifolds. As it is not possible to take a fluid temperature readings directly at the entrance and exits to the microchannels without obstructing the fluid flow, the fluid temperature is taken from over the pressure tappings on the inlet (1.5mm from entrance) and outlet (3mm from exit), as shown in Figure 4.19. In order to account for the manifold heating effect the heat transferred to the fluid from the manifolds between the thermocouples on the microchannel test sample was calculated and subtracted from the overall heat transfer measured by the fluid temperature thermocouples.

To calculate the heat transferred from the manifolds to the fluid the same process used to find Nusselt numbers for the rectangular channels was used to find Nusselt numbers for the manifolds, incorporating the data in Table 3.2 & Table 3.3. and also the Muzychka and Yovanovich correlation *(Eqn. 15)* . Using the manifold surface and fluid temperatures a value for the heat transfer coefficient was established and from this, values for the temperature of the fluid at the entry and exit points to the channels were found. These temperatures were then used to find the heat transfer from the microchannels and the Nusselt numbers for each test sample. This method ensures that the results from each heat transfer experiment are exclusively based on the energy transfer through the microchannel surface to the fluid.

6.5. Result Processing with MATLAB

The MATLAB code written for the previous sections is quite extensive and is therefore include on the CD attached with this report. The list of *Programs* and *Commands* used to calculate the experimental and theoretical results are as follows.

1) *initializ.m* – This initialises the variables needed for the *mc.m* program.
2) *mc.m* (Up to break point) – Sets the channel size and the heat transfer area (3 walls etc.) for result processing.
3) *Result_processsor_Nu.m* - Processes the experimental data points.
4) *mc.m* (Complete run) – This run calculates the theoretical results for each o the averaged experimental points.
5) *Tempss.m* – Stores the nominal experimental temperatures and results prior ('nominalresults') to uncertainty calculation by *TempTweak.m.*
6) *TempTweak.m* – Alters the nominal experimental temperature results to produce upper and lower values of uncertainty.
7) *upperresults=[output dataOut];* - this function saves the output files from (3 & 4) to a variable called 'upperresults'.
8) *lowerresults=[output dataOut];* - this function saves the output files from (3 & 4) to a variable called 'lowerresults'.
9) *Finaloutput.m* – Saves the 'upperresults', 'nominalresults' and 'lowerresults' variables to a text file which can be imported into Excel.

In order to produce a full set of theoretical and experimental results including the upper and lower uncertainties the following procedure must be completed. To calculate the nominal results the programs (1-5) are run with channel's size set to the nominal size. In the case of program (3) the *TempTweak.m* setting was selected by pressing enter. For the lower limit of uncertainty the following programs and functions are run in order (6, 2, 3, 4 and 8). For programs 2 & 4 the channel size was set to the nominal channel size plus 1.96 standard deviations and the *TempTweak.m* setting was selected in (3) by inputting 1. To calculate the upper limit of uncertainty the programs and functions were run as follows (6, 2, 3, 4 & 7), the channels size was equal to the nominal size minus 1.96 standard deviations for 2 & 4, and again the *TempTweak.m* setting was selected in (3) by inputting 1. Once each run had been completed the *finaloutput.m* (9) was initiated and three sets (upper, lower and nominal results) of theoretical and experimental data were sent to a text file. This information was then imported into Excel allowing the result data to be plotted as shown in section 7.0.

7.0 Results & Discussion

In this section the results of the previously described experiments are shown. These results were taken using real time data acquisition at 4 samples per second. This method is most commonly used at present as the acquired results can be process relatively quickly in comparison to manually recording data, as previously used (Eason, 2005). Continuously logging experimental data can also provide a greater insight into the actual process being measured. As shown in Figure 11.14 & Figure 11.15, where a long test, monitoring the Mass Flow Rate and the Pressure drop was performed to establish the tame taken for the system to reach a steady state. In both measurements a steady state condition was reached after the system had been running for 15 to 20mins. However it should be noted that both plots follow the same path and therefore in experiments which took longer to stabilise it was safe to assume that the system was at a steady state if the variations in each reading were equal and infinitesimal in comparison to the actual reading.

7.1. Channel Measurements

The results of the area measurements along with the target dimensions used for the manufacturing process for both channel types can be found below in Table 7.1. The uncertainties are quoted using the ±1.96 standard deviations from the nominal value. In the rectangular channel (*DRIE*) measurement the largest deviation from the target dimensions was found in the channel height which created an aspect ratio almost equal to one. The uncertainty for this measurement also contained a ±4.6% deviation from the nominal value, this deviation was also carried over to the cross sectional area resulting in an uncertainty of ±4.2%

For the trapezoidal channels (*KOH*) both the nominal channel height and width were approximately 3.25% and 3.45% over the initial target dimensions therefore the hydraulic diameter and cross sectional area were also larger than the expected values. It should also be noted the base width (W_b) of these channels seems to change considerably from channel to channel and an uncertainty of ±41% was generated. During the channel measurement it could be seem that the tip of each trapezoidal channel was slightly curved and not perfectly straight as expected. Therefore an approximated width was taken for W_b. Any large uncertainties recorded could be attributed to poor judgement when applying the measurement points to determine the

average cross sectional area or simply due to focusing errors between the calibration slide and channel images.

Table 7.1 Details the results of the channel measurement for both microchannel samples.

	n	*H* (μm)	*W* (μm)	W_b (μm)	*L* (mm)	*Pitch* (μm)	D_h (μm)	*CSA* (mm^2)
KOH *(trapezoidal)*	22	413.02 ± 10.82	605.19 ± 20.2	24.66 ± 10.1	29.86 ± 0.01	690	317.78 ± 3.48	0.1306 ± 0.0037
TARGET KOH	22	400	585	***N/A***	30	700	305.1	0.1208
DRIE *(rectangular)*	22	305.88 ± 14.15	304.67 ± 5.05	***N/A***	30.02 ± 0.01	700	307.49 ± 7.93	0.0932 ± 0.0039
TARGET DRIE	22	320	300	***N/A***	30	700	309.7	0.096

7.2. Pressure Flow Data

Firstly the experimental pressure drop (Pa) taken while heat was applied to the channels for both the DRIE and Wet Etch (*KOH)* samples was plotted against the corresponding mass flow rate (g/s) as shown in Figure 7.1 & Figure 7.2. All of these experimental and theoretical results were temperature compensated and are therefore are denoted by *'_comp'*

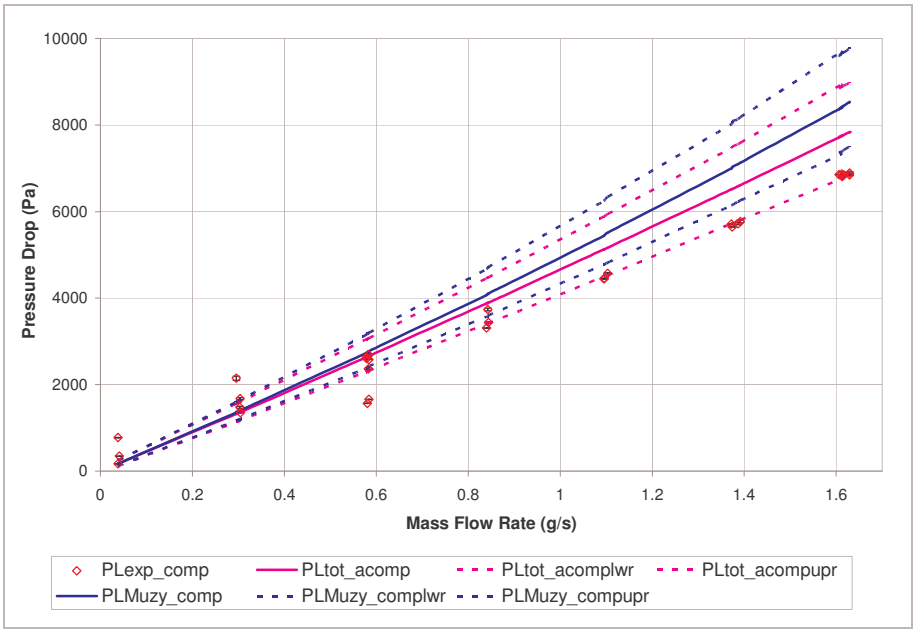

Figure 7.1 Details the pressure drop across the DRIE channels for different mass flow rates (Eason *et al* 2007).

The experimental results are compared to two theoretical correlations (Rohsenow *et al* 1985; and Muzychka and Yovanovich, 2004) the first is based on the findings of (Shah and London, 1978) and Darcy's equation (*Eqn. 7*). This correlation also required area compensation and so it is denoted by '*PLtot_acomp'*. The second correlation (*PLmuzy_comp)* is already area compensated as the friction factor calculations are based on the square root of the cross sectional area, and again the pressure drop was calculated using Darcy's equation. In each Pressure drop plot the theoretical upper and lower uncertainty curves are shown along with the experimental uncertainty, however these experimental values were quite small and are not clearly visible on the graphs.

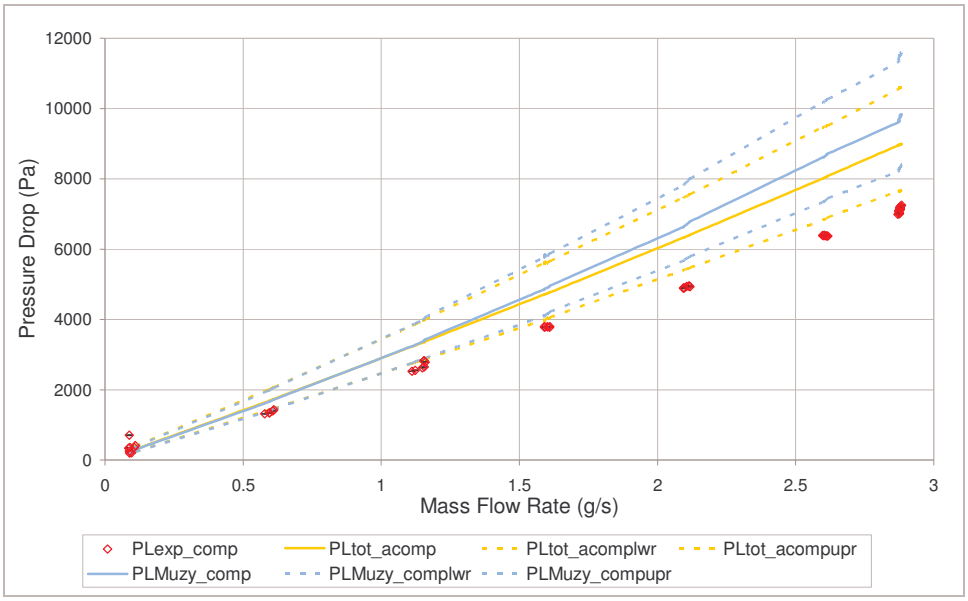

Figure 7.2 Shows the experimental and theoretical Pressure drop across the Wet Etch channels at the different flow rates (Eason *et al* 2007).

In the both cases the experimental pressure drop lay slightly below the theoretical values. The DRIE results in Figure 7.1 observed some point scatter at the lower flow rates, however after 0.8g/s the pressure drop lay on the lower uncertainty of the Rohsenow correlation until the maximum reading from the pressure transducer. The Wet etch channels emphasise a much lower pressure drop for the same flow rate as the DRIE channels, however the results in Figure 7.2 show the experimental values falling along a slope slightly lower than the Rohsenow correlation. In the previous work (Eason, 2005) the experimental pressure drop correlated well with theory for the DRIE channels and for the Wet etch channels a deviation occurred which was approximately equal to the errors encountered in this experiment. These comparisons would suggest that the area measurements for DRIE channels could be inducing this

deviation, as the previous experiments recorded a cross sectional area of 0.101mm^2 for the DRIE channels and 0.126mm^2 for the Wet Etch channels. Both the current and previous experimental curves seem to have recorded the same pressure drops as shown above (Figure 7.1 & Figure 7.2) for the corresponding mass flow rates, however the previous theoretical correlations lie much lower than current correlations. This is almost certainly due to the fact that the Darcy's equation (*Eqn .7*) is inversely proportional to the area squared (*Eqn. 23)* and therefore the smaller the area the greater the pressure drop.

In order for the experimental data to be compared easily with other experimental data in literature it is quite common to represents the pressure flow results for each experiment in a graph plotting the product of the friction factor and the Reynolds's number (*fRe*) values against the Reynolds's number (*Re*). The following graphs shown in Figure 7.3 & Figure 7.4 detail the experimental and theoretical *fRe* values for the DRIE and Wet etch channels used in this work plotted against the corresponding *Re* numbers respectively.

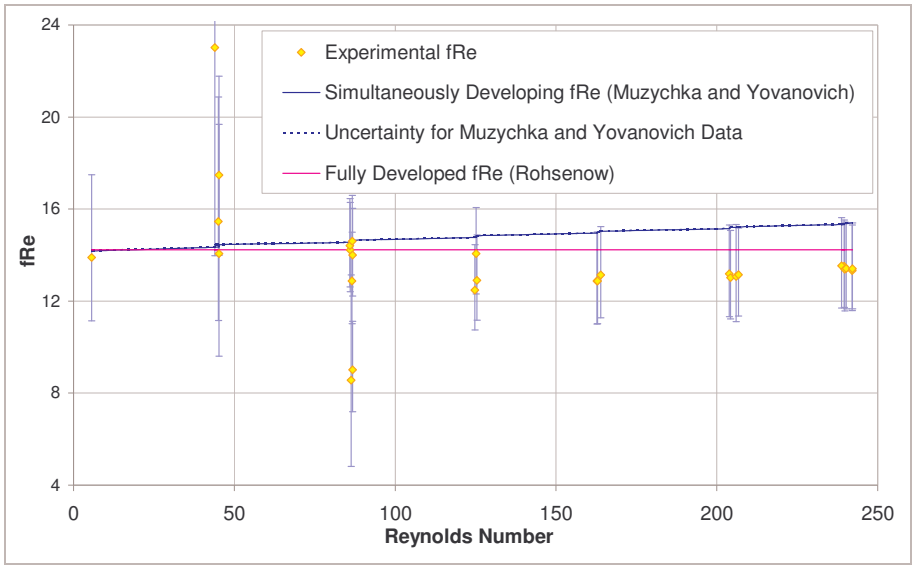

Figure 7.3 Details the Friction Factor by the Reynolds Number for the DRIE channels (Eason *et al* 2007) (points omitted for clarity see appendix).

It is important to note that two of the experimental *fRe* values for the low *Re* numbers were omitted from Figure 7.3 to provide a smaller scale on the y axis thus showing the data in more detail, the full graph is shown in Figure 11.16 in appendix D of section 11.0.

Again both the experimental values for the DRIE and Wet Etch channels are considerable lower than the theoretical correlations of Rohsenow and Muzychka. The

fRe values for the DRIE channels (Figure 7.3) show quite scattered results with large uncertainties up to a *Re* number of 100 after which the results stabilise to follow a path much like the Muzychka correlation however this curve is offset by constant error of 2 and the uncertainties are still remain quite large. The uncertainty for these experimental measurements are calculated by working backwards from Darcy's equation (*Eqn.* 7) to discover the friction factor and then multiply it by *Re*. This method of calculation can result in a more cumulative uncertainty than the theoretical correlations and As these uncertainties create error bars which cross both theoretical correlations it is simply not possible to suggest that there is a significant deviation from the conventional theory (Eason *et al* 2007) and therefore the data must be subject to some form of experimental error which is most likely related to the area measurement as previously stated.

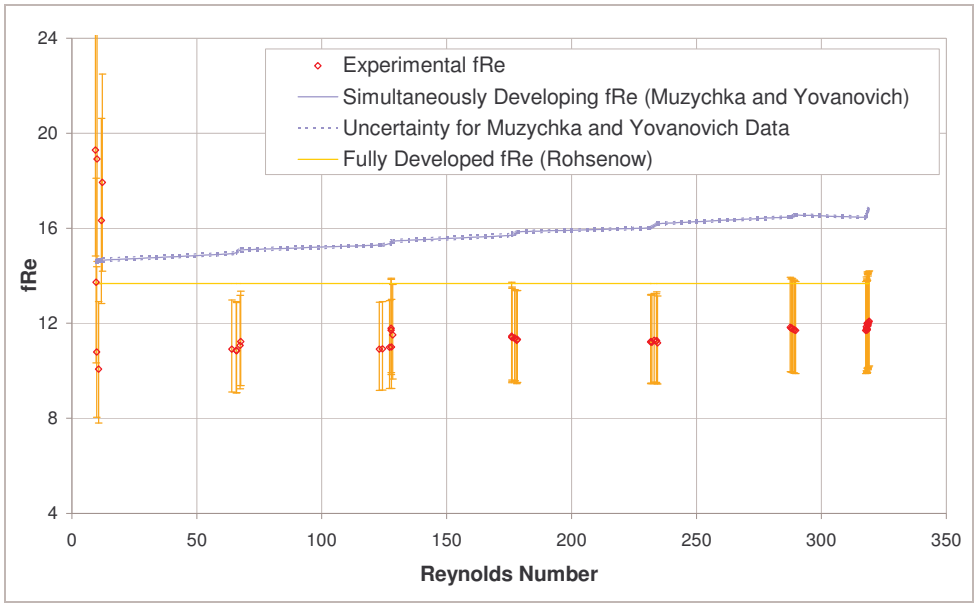

Figure 7.4 Details the Friction Factor by the Reynolds Number for the Wet Etch Channels (Eason *et al* 2007).

In the case of the Wet Etch channels there was also a presence of strong variations in the *fRe* values at very low *Re.* These values correspond to mass flow rates of around 0.1g/s which is extremely low and often makes experimental measurements quite difficult to achieve accurately. After this point the experimental data tends to level out with the majority of data points for each experimental *Re* number falling close together. These data points still fall considerably lower than the theoretical calculations however the uncertainty remains consistent throughout the rest of the result data with error bars error bars only barely crossing the Rohsenow correlation and so it would be feasible to suggest that these results show a significant deviation

from the theoretical correlation. Although since the DRIE results are quite poor it would appear that these experimental deviations could be caused by the experimental system rather than the actual behaviour within the microchannels.

Possible reasons for these errors are most likely linked to the to the area measurements which were taken using an optical microscope, whereas in the previous work (Eason, 2005) a Scanning Electro Microscope was used (which provides scaling for each image taken). The previous experiments produced extremely good pressure drop measurements that matched the correlations extremely well for the DRIE channels. Another area to investigate would be the pressure measurement, the Setra pressure transducer was tested against a Valydine transducer (from previous work) with both unit placed in parallel and it was proved to be more accurate however the application of the pressure through the burettes could easily create small variations in pressure could be attributed to poor levelling techniques and the another method of pressure application should be pursued.

7.3. Heat Transfer Data

The initial experimental results for the heat transfer characteristics of the DRIE and Wet Etch channels are shown on Nusselt number against Reynolds's number plots in Figure 7.5 & Figure 7.6 respectively. The DRIE channel results showed the experiment results dispersed throughout the graph with some numbers proving to be negative however once the manifold heating effect was applied to each experimental point the data converged to a single line of points as shown in Figure 7.5.

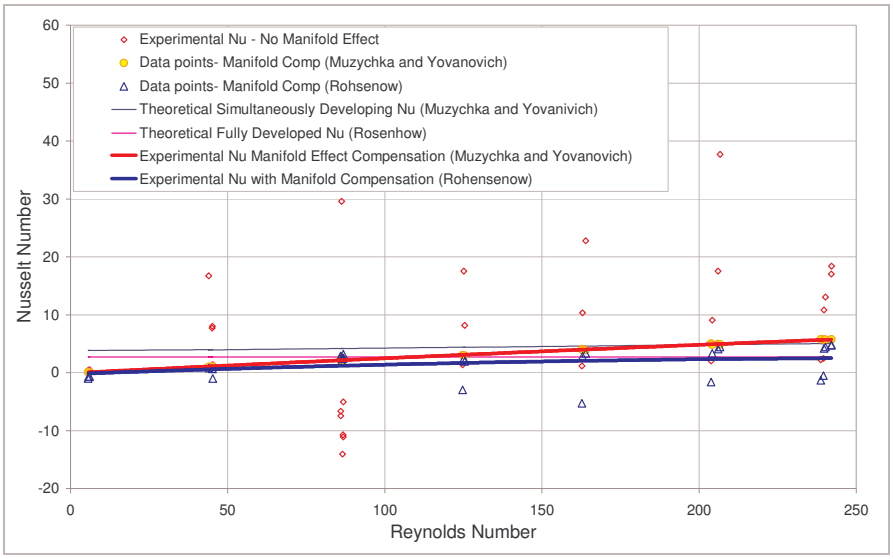

Figure 7.5 Shows the manifold heating effect on the experimental Nusselt Number for the DRIE Channels (Eason *et al* 2007).

The same results were also recorded for the Wet Etch channels with some dispersion taking place at low Reynolds's numbers after which all the experimental numbers converged to form a curve of negative values. Once the manifold effect was taken into account these values became positive with all points falling closely to the curve as shown in Figure 7.6.

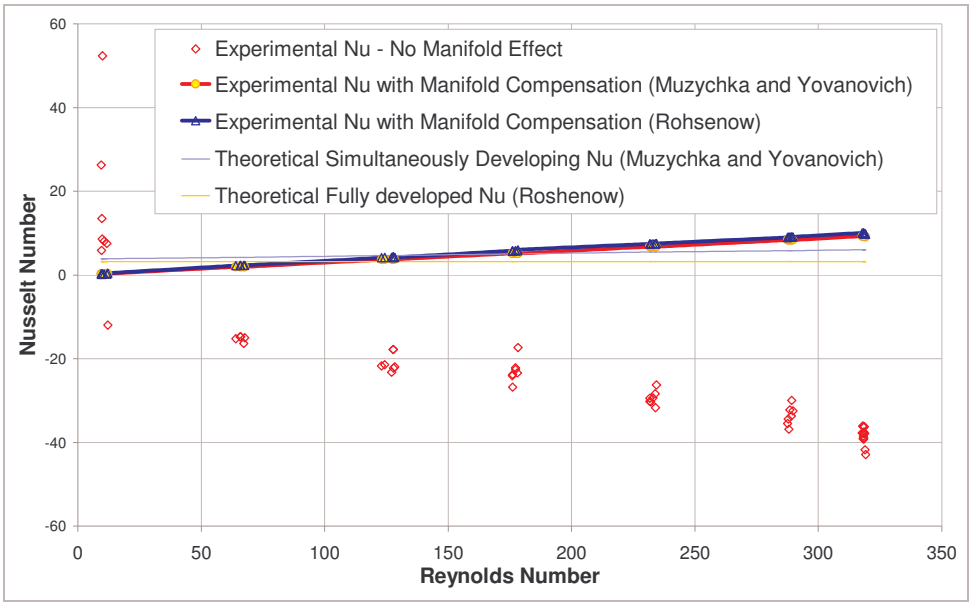

Figure 7.6 Shows the manifold heating effect on the experimental Nusselt Number for the Wet Etch Channels (Eason *et al* 2007).

The theoretical Nusselt numbers were calculated using two different correlations, the first used was the Rohsenow correlation (Schmidt, 1978; Shah and London, 1978) for fully developed flow which consists of two sets of data, one for each channel shape and was taken from (Rohsenow *et al* 1985). The second correlation, the Muzychka correlation was derive for simultaneously developing flow in non-circular ducts and therefore could be applied to both channel types to calculate the theoretical Nusselt number using (*Eqn 15)*. However the heat transfer results produced after the manifold effect was taken into account showed a strong linearity between the Nusselt number and Reynolds's number for both channel types. This unexpected result made it impossible to make a comparison between the theoretical and experimental results.

The experimental results for the DRIE channels shown more clearly in Figure 7.7 shows a strong linear relationship between the experimental Nusselt numbers based on the Muzychka correlation and the corresponding Reynolds's numbers. The linear relationship was not so apparent in the Nusselt numbers based on the Rohsenow correlation as some of these values became negative after the compensation for

manifold heating effect was implemented. However the majority of the positive points seemed to follow the trend of the experimental Muzychka points. Almost no comparison can be made with the theoretical values as the results seem to be following a very steep gradient.

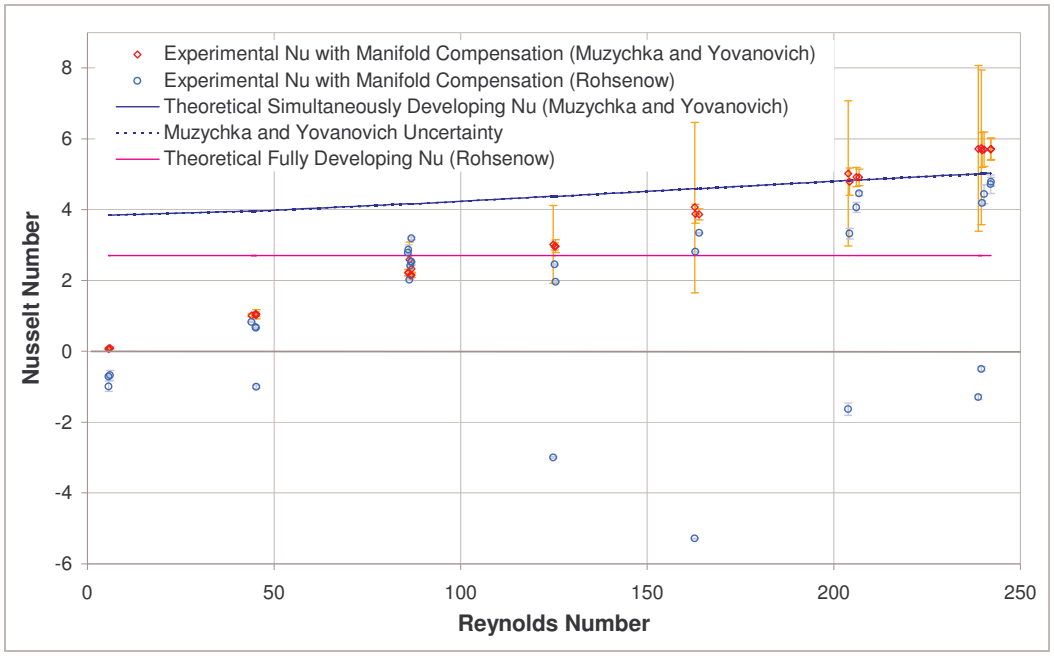

Figure 7.7 Details the results of the Nusselt Number vs Reynolds number plot for the DRIE Channels (Eason *et al* 2007).

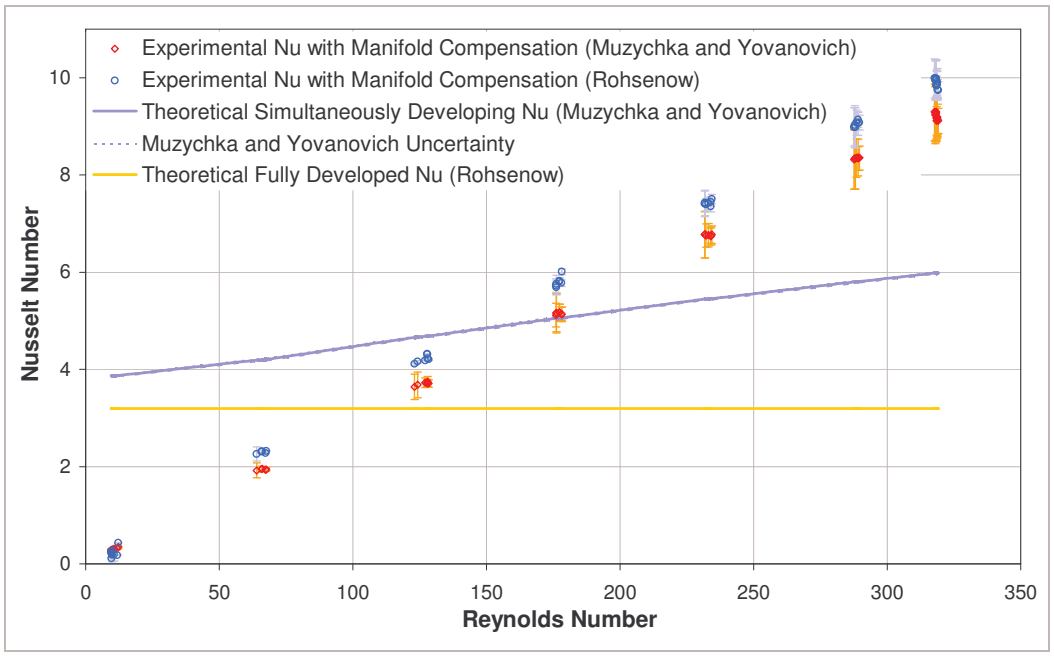

Figure 7.8 Details the result of the Nusselt vs Reynolds Number plot for the Wet Etch Channels (Eason *et al* 2007).

For the Wet Etch channels the experimental Nusselt number results shown in Figure 7.8, demonstrate an even stronger linear dependence on the Reynolds number and bares no resemblance to the theoretical correlations. However it is interesting to note that the experimental results based on the Muzychka correlation produce a slightly more conservative estimation of the Nusselt number than the Rohsenow correlation.

A search through the correlations used in previous experiments from (Lee *et al* 2005) found that the Sieder-Tate correlation (*Eqn. 27)* provided a slightly better comparison to the DRIE channel results the equation

$$Nu_{Sieder-Tate} = 1.86\left(\frac{\mathrm{Re}\,\mathrm{Pr}\,D_h}{L}\right)^{1/3}\left(\frac{\mu_f}{\mu_S}\right)^{0.14} \qquad \textit{(Eqn. 26)}$$

This equation was originally derived for circular channels with simultaneously developing flow however it has often been used for non-circular tubes by substitution of the hydraulic diameter (Lee *et al* 2005). The result of the Sieder-Tate correlation can be seen below in Figure 7.9, the correlation has a slightly better representation of the experimental results in comparison to the previous correlations. However it is not an ideal representation and the correlation did not compare well with the Wet Etch channels.

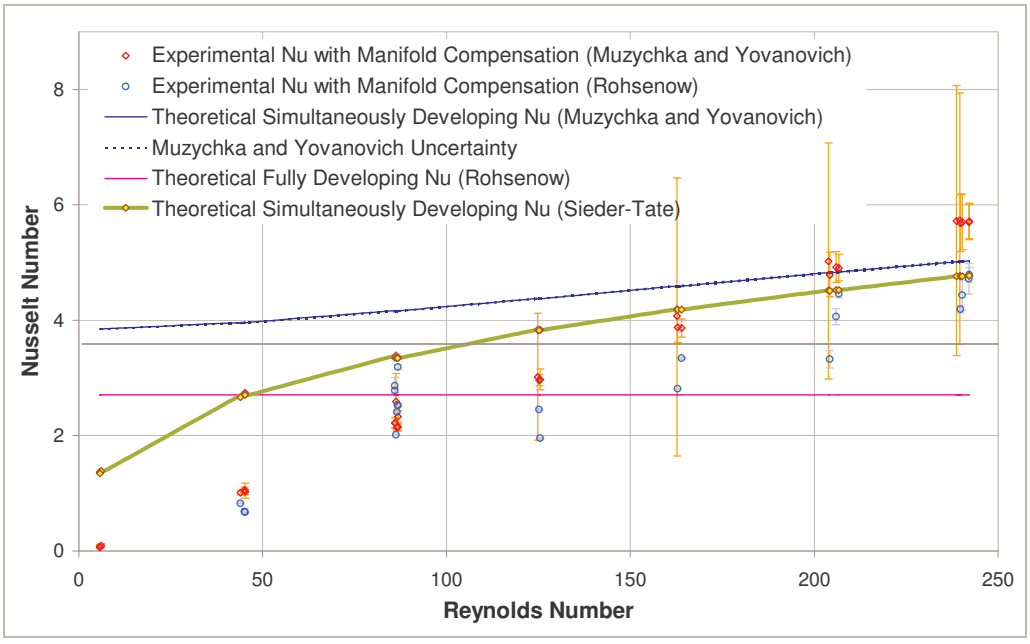

Figure 7.9 Details the addition of the Sieder-Tate correlation for the DRIE channel results.

As the pressure flow data showed no sign of an early transition to laminar flow it must be concluded that the behaviour of the experimental results was not evidence of new experimental activities but most likely a consequence of either the test system or the methods used to acquire the result data (Eason *et al* 2007).

For DRIE channels the deviation in the results from the theoretical correlations is almost certainly related to the area measurement as previously discussed. However in the case of the Wet Etch channels, these unusual results could be attributed to the lack of appropriate theoretical correlations. In both the Rohsenow and Muzychka correlation used for these experiments the assumption was made that all walls were heated on the trapezoidal channels, which is not the case and be the could the cause of unexpected heat transfer results . It should also be note that the values for the *fRe* and the Nusselt numbers were taken from the data in Table 3.2 which depends on the acute corner angle and also the channel height divided by the base width ($^{H}/_{Wb}$). As W_b was in fact not perfectly straight and generally formed a curved shape, an averaged length measurement was required. As shown earlier in section 7.1 it proved quite difficult to accurately measure the base width (W_b) length, and resultant measurements observed uncertainties of almost ±41%. These large uncertainties could easily have affected both the *fRe* and *Nu* results.

In previous research numerical modelling has provided accurate results in comparison to experimental work (Lee *et al* 2005; Qu and Mudawar, 2002) and therefore to establish if the system is capable of measuring accurate results a numerical study using CFD should be performed.

8.0 Conclusions

- The experimental Pressure Drop (P_L) and fRe values were considerable lower than the theoretical predictions for simultaneously developing and fully developed flow for both channel types. The DRIE data could not prove any significant deviation from theory however for the Wet Etch results the data in both cases showed a rather significant deviation from the theoretical results
- As a result of the poor Pressure Drop results for the DRIE channels, the dimensions were investigated and compared to the previous work (Eason, 2005) where good pressure drop correlations were observed. It was suggested that the optical microscope could have created some scaling errors caused by focusing each image and in future a Scanning Electron Microscope should be used.
- During the area measurement it was discovered the base width W_b was in fact a curved shape and was subject to huge uncertainties caused by the averaging of its length. It was suggested that this discrepancy caused the variations between the experimental and theoretical results for the Wet Etch channels.
- In order to provide accurate heat results it is imperative that the effect of manifold heating is taken into account, as huge errors are recorded in the uncompensated experimental results.
- The results from the heat transfer experiments showed the experimental Nusselt number having a strong linear relationship with the Reynolds number which has not been reported before in literature and it was therefore concluded that this unusual deviation from theory was most likely the cause of the experimental system or the methods used to acquire the experimental data
- For the Trapezoidal channels it was recommended that more accurate theoretical correlations should be discovered to represent the unique wall heating conditions.
- During testing it was discovered that the time taken for the system to reach steady state took in the region of 15 -20 minutes.
- Incorporating the modifications for the experimental apparatus and the data acquisition reduced the uncertainty in the results and allowed the data to be processed more efficiently.

9.0 Future Work

- To measure the area of the recently tested microchannel samples using a Scanning Electron Microscope to determine if the current results taken using an optical microscope are valid
- To perform numerical analysis of the existing system using CFD to discover if the system can accurately measure heat transfer and pressure flow results, and if so test the validity of the current results.
- At present the limits of the existing rig have been tested and so for the future it would probably be best to develop other methods of the performing the same experiments with a greater accuracy. Such as locating the pressure tapping in the actual microchannels and possibly placing thermocouple along the length of the channel to discover the temperature gradients involved in this experiment.
- If a new system was to be designed considerations should be put in place to allow easier thermocouple positioning and mounting or incorporate different temperature measurement techniques (for example using infra-red imaging). The application of heat to the system should also be reviewed, possibly using a thin film resistor mounted on the back of the test sample.

10.0 References

- Belhardja, S., Mimounia, S., Saidanea, A., Benzohrab, M. (2003), 'Using microchannels to cool microprocessors: a transmission-line-matrix study' Microelectronics Journal, 34, 247-253.
- Bucci, A., Celata, G. P., Cumo, M., Serra, E., Zummo, G. (2003) 'Water single phase fluid flow and heat transfer in capillary tubes', editiors, Microchannel and Minichannels: Proceedings of the First International Conference, Rochester, New York, 24th – 25th April 2003, Place of publication: Publisher, ICMM2003 – 1037
- Cooligy (2006) Microstructure Cooling [online image], Available: http://www.cooligy.com/micro_structure_cooling.html, [accessed 20th November 2006].
- Dutch, S. (1997) *Miller Indices*, [online] available: http://www.uwgb.edu/DutchS/symmetry/millerdx.htm [accessed 3 April 2007]
- Eason, C.J. (2005), The Measurement of Experimental Pressure Drop and Heat Transfer from Microchannels in Silicon and Plastic, Thesis (PhD), University of Limerick.
- Eason, C. J., O'Keeffe, N. W., Enright, R., Dalton, T. (2007) 'DRAFT: On correlating experimental pressure flow and heat transfer measurements from silicon microchannels with theoretical calculations', paper under review for the ASME-JSME Thermal Engineering Summer Heat Transfer Conference, Vancouver, British Columbia, Canada, 8-12 July 2007.
- Harms, T. M., Kazmierczak, M. J., Gener, F. M. (1999) 'Developing convective heat transfer in a single-phase microchannel heat sink, International Journal of Heat and Mass Transfer, Volume 45, 2549 – 2565.
- International Technology Roadmap for Semiconductors {ITRS}, (2006) '2006 Update – Assembly and Packaging', [online], available: http://www.itrs.net/Links/2006Update/2006UpdateFinal.htm [accessed: 16th March 2007].
- Judy, J., Mayes, D., Webb, D. W. (2002) 'Characterization of frictional pressure drop for liquid flows through microchannels', International Journal of Heat and Mass Transfer, Volume 45, 3477 – 3489.
- Lee, P., Garimella, S. V., Liu, D. (2005) 'Investigation of heat transfer in rectangular channels', International Journal of Heat and Mass Transfer, Volume 48, 1688 – 1704.
- Markoff, J. (2004), 'Intel's Big Shift After Hitting Technical Wall', The New York Times [online], 17 May 2004, available: http://www.nytimes.com/2004/05/17/business/17intel.html?ex=1400212800&en=482e56801aa02ede&ei=5007&partner=USERLAND [accessed 21 March 2007]
- Mendelson, H., (1979) 'Moore's Law', Prepared for the Encyclopaedia of Computer Science, 1979. (Quoted on http://www.thocp.net/biographies/papers/moores_law.htm). [accessed 20th March 2007]

- Muzychka, Y.S., Yovanovich, M.M. (2004) 'Laminar Forced Convection Heat Transfer in the Combined Entry Region on Non-Circular Ducts' Journal of Heat Transfer, Transactions of the ASME, February 2004, Vol 126, 54-61
- National Instruments (2007) PCI-6229 & SCB-68 [Online image], available: http://sine.ni.com/nips/cds/view/p/lang/en/nid/14124, [accessed 1st April 2007]
- Peng, X.F., Peterson, G.P. (1995a) 'Convection heat transfer and flow friction for water', International Journal of Heat Mass Transfer, 39(12), 2599-2608.
- Peng, X.F., Peterson, G.P. (1995b) 'The effect of thermofluid and geometric parameters on convection of liquids through rectangular microchannels', International Journal of Heat Mass Transfer, 38(4), 755-758.
- Phillips, R. J., (1990) 'Microchannel Heat Sinks', Advances in thermal modelling of electronic components and systems, Volume 2.
- Prasher, R.S., Chang, J., Sauciuc, I., Narasimhan, S., Chau, D., Chrysler, G., Myers, A., Pristic, S., Hu, C. (2005) 'Nano and Micro Technology-Based Next-Generation Package Level Cooling Solutions', Intel Technology Journal [online], 9(4), 285-296, available: http://www.intel.com/technology/itj/archive/2005.htm [accessed 21st November 2006].
- Qu, W., Mudawar, I. (2002) 'Experimental and Numerical of Pressure Drop and Heat Transfer in a Single Phase Microchannel', International Journal of Heat Mass Transfer, 45, 2549-2565.
- Rohsenow, W.M., Hartnett, Ganić, E.N., eds. (1985) Handbook of Heat Transfer Fundamentals, 2nd ed., New York: McGraw-Hill Book Company.
- Shah, R.K., London, A.L. (1978) 'Laminar Flow Forced Convection in Ducts' Supplement 1 in Advances in Heat Transfer, Ed. Irvine, T.F. and Hartnett, J.P., Academic, New York 1978.
- Schmidt, F.W., (1978) presented in Shah, R.K. and London, A.L., 'Laminar Flow Forced Convection in Ducts', Academic, New York, 1978.
- Tuckerman, D. B., Pease R. F. W. (1981) 'High-Performance Heat Sinking for VLSI', IEEE Electron Device Letters, EDL-2(5), 126-129.
- Viswanath, R., Wakharkar, V., Watwe, A., Lebonheur, V. (2000) 'Thermal Performance Challenges from Silicon to Systems' Intel Technology Journal [online], 4(3), 1-16, available: http://www.intel.com/technology/itj/archive/2000.htm [accessed 5th March 2007]
- Wu, P., Little, W. A. (1983) 'Measurement of friction factors for the flow gases in very fine channels used for microminature refrigerators', Cryogenics, 24, 273-277.

11.0 Appendices

A. Conference Paper

B. LabVIEW Programs

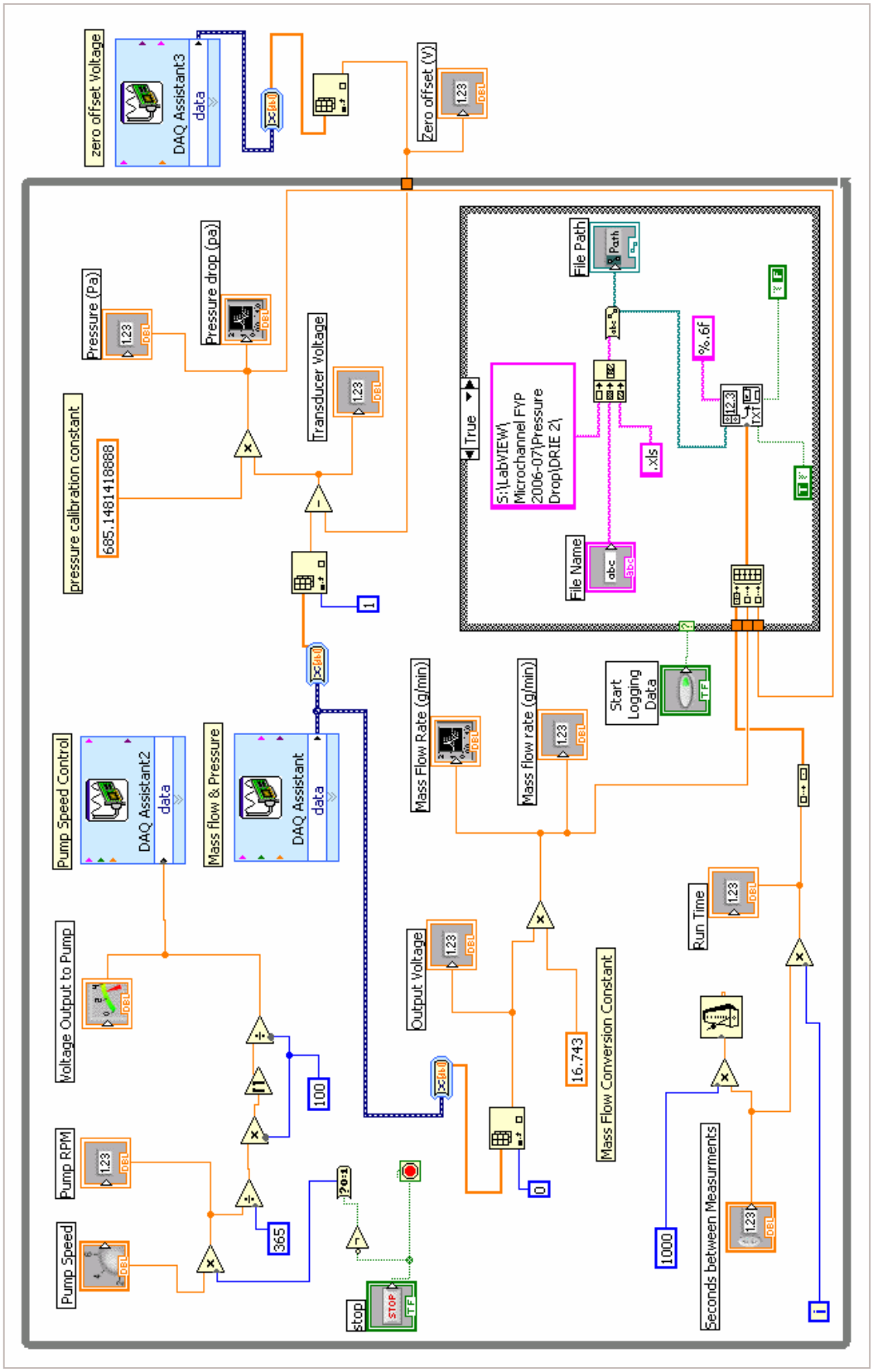

Figure 11.1 Details the LabVIEW block diagram for the pressure drop experiments

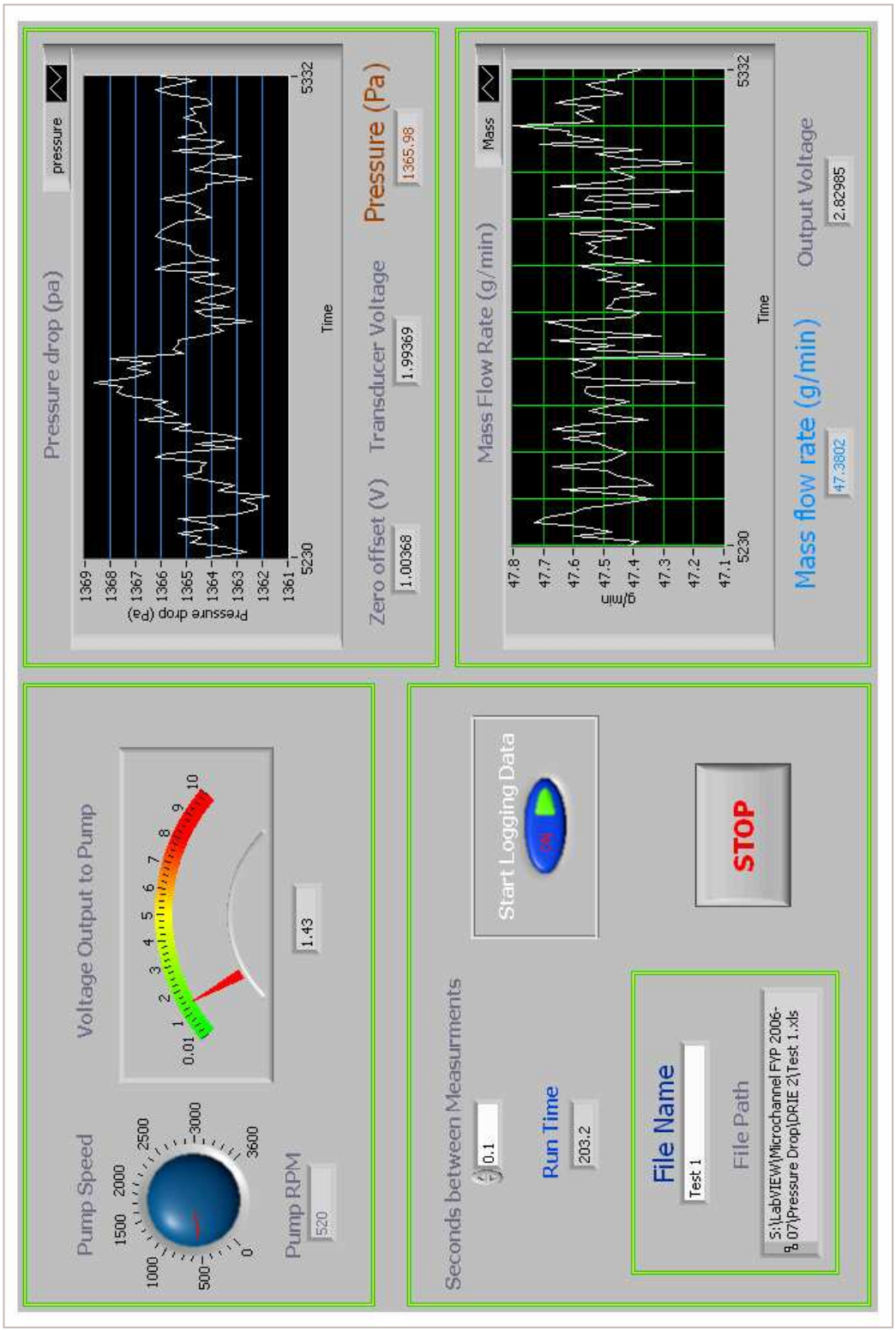

Figure 11.2 Shows the Front panel display in LabVIEW for the pressure drop experiments.

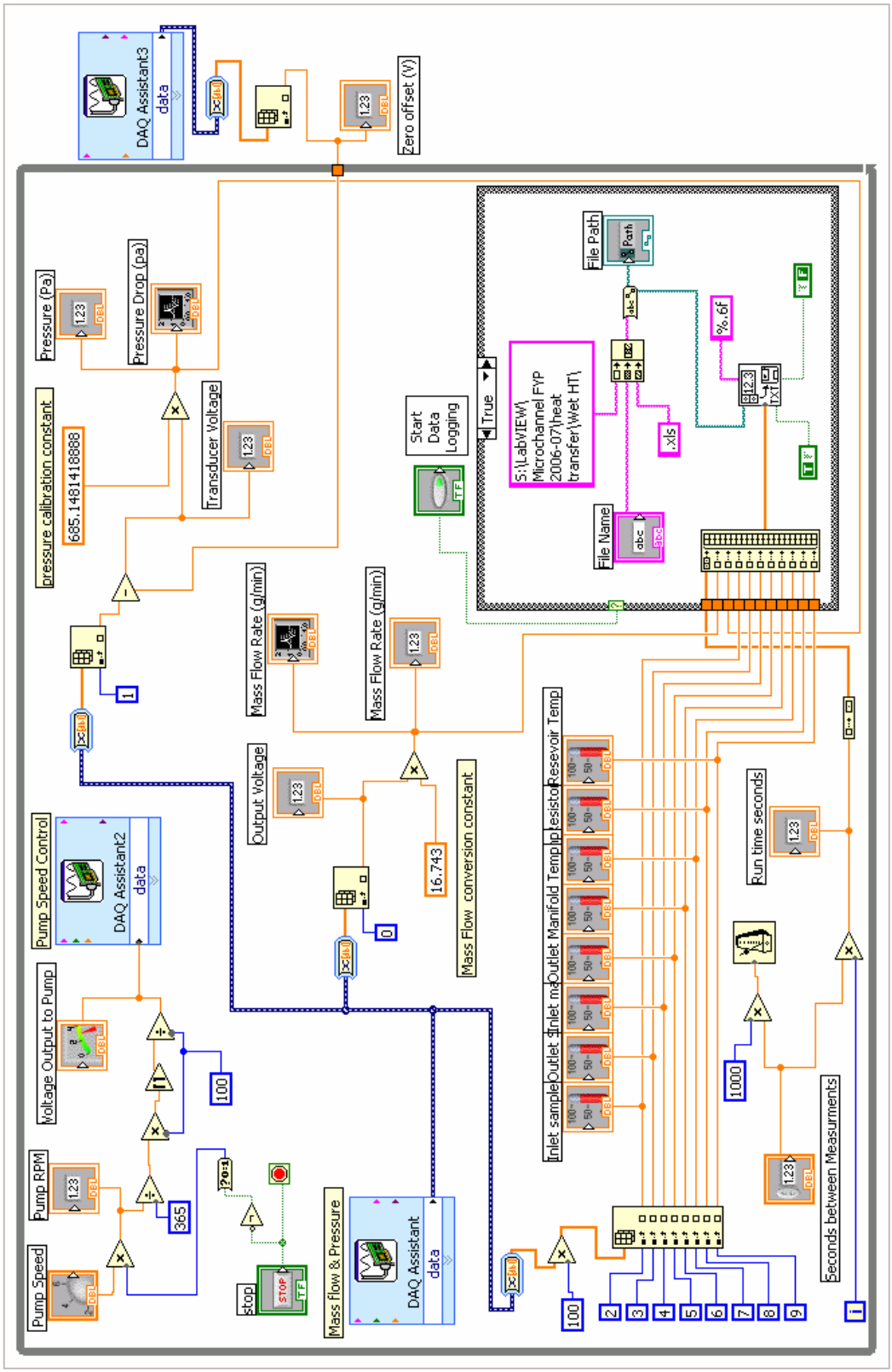

Figure 11.3 Details the LabVIEW block diagram used for the heat transfer experiments.

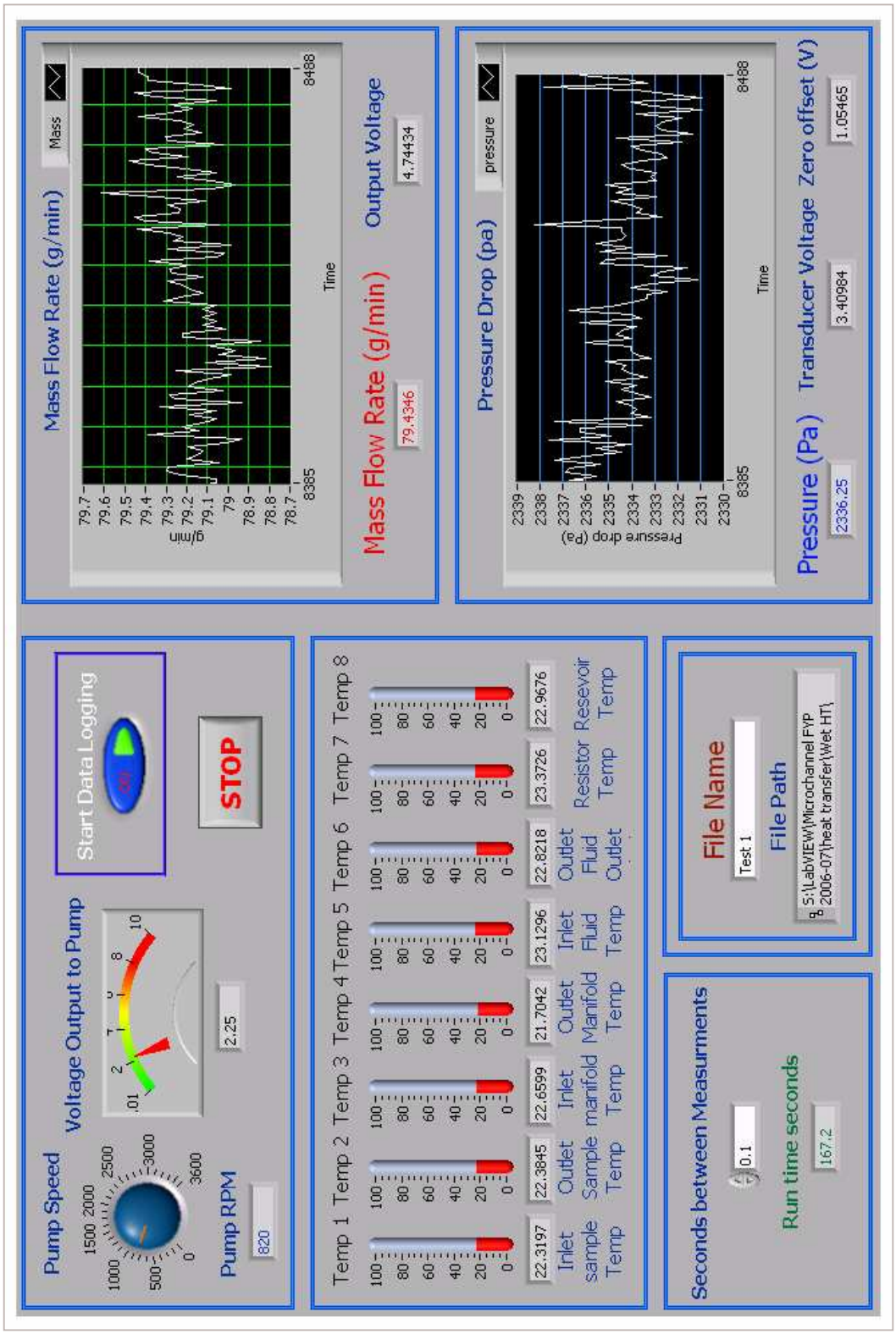

Figure 11.4 Shows the Front panel display in LabVIEW used for the heat transfer experiments.

C. Microchannel Measurement

In this section the results of the image editing used to calculate the area of the channels are shown. It should be noted that images for the DRIE channels are not as clear because the shape of the channel did not permit adequate light to shine through the channel from the light source below. However these images produced a much clearer outline of the channel in comparison to those with the light source being applied from above. As shown in Figure 11.5, the edges at the entry to the DRIE channels are quite rough as a result of the dicing blade which cut the samples out of the silicon wafer. These rough edges did not improve with sanding and provided very poor outline of the channel wall at high magnifications, however looking past these edges the channel walls seemed to be relatively clean and therefore it is safe to presume that the edges of the DRIE channels are as shown in Figure 11.6 & Figure 11.7

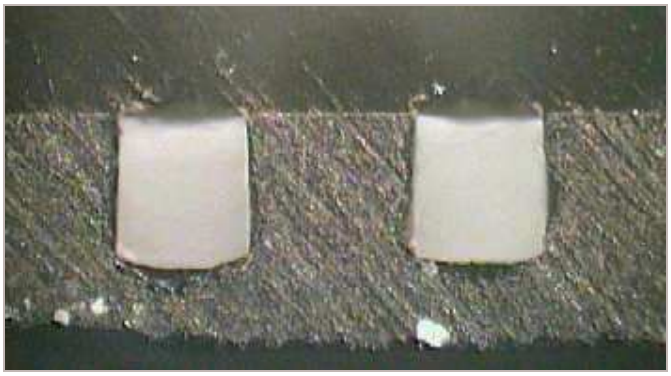

Figure 11.5 Shows the rough edges of two DRIE channels at a lower magnification

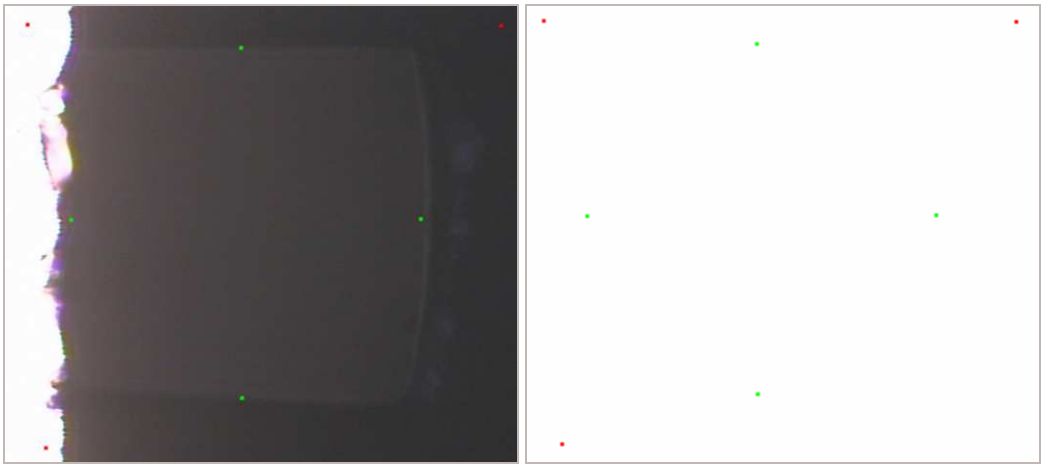

Figure 11.6 Shows the layered image (left) **of the DRIE channel and also the gif file image** (right) **analysed by MATLAB for the height and width measurements**
(note the size of coloured points have been increased for clarity)

In Figure 11.6, method for retrieving height and width lengths from the DRIE channels is shown. This method was used for the majority of the channels and points were placed strategically to produce a rectangle which accurately represented the channels CSA.

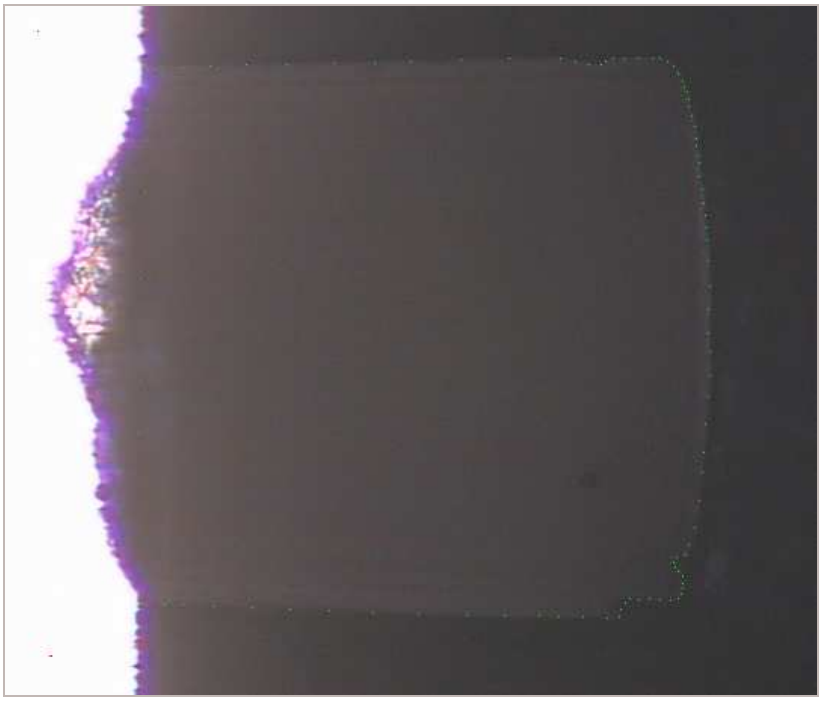

Figure 11.7 Shows a DRIE channel image with the coloured pixels added on a separate layer.

Figure 11.8 Shows the gif file for Figure 11.7 which was scanned by the MATLAB program.

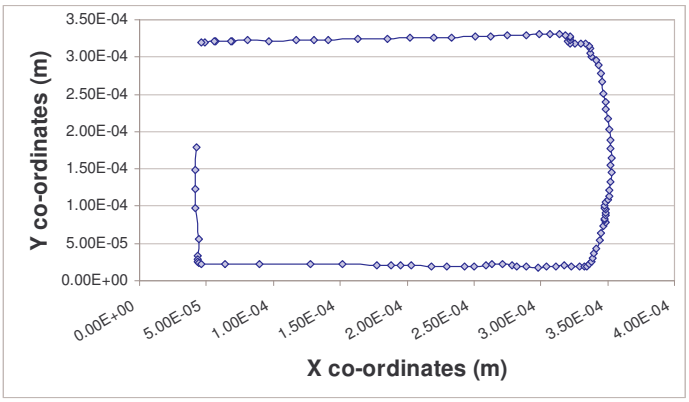

Figure 11.9 Details the DRIE channel outline points scanned by MATLAB and rearranged in the correct order.

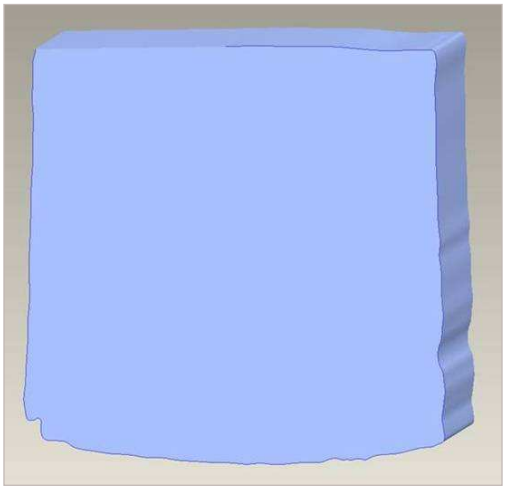

Figure 11.10 Shows the ProEngineer extruded cross section of a DRIE channel

The gif file scanned by the MATLAB program produces the green pixels points with accurate co-ordinates from the top left hand corner. However the program scanned the channel image from left to right and thus all the points had to be rearranged before being exported to ProEngineer. From here a spline curve was added to the points and the surface was extruded (Figure 11.10). The cross sectional area was discovered using the measure function which calculates the area of a selected surface.

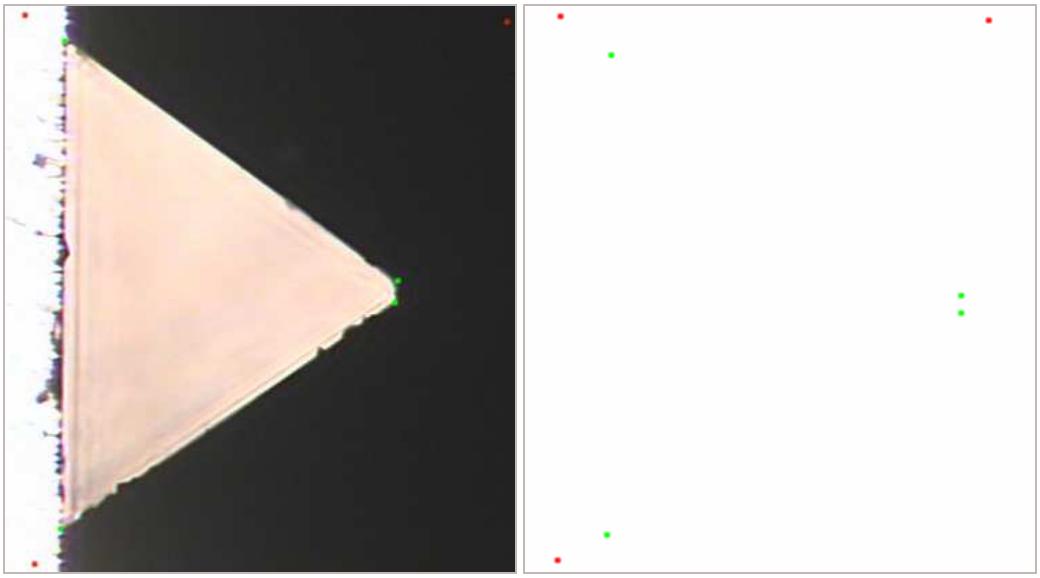

Figure 11.11 Details the method used to provide a rough calculation for the trapezoidal area. Layered image (left) **& gif file** (right) (note the size of coloured points have been increased for clarity)

Again for the majority of the channels the four point method was used with six channels receiving full point mapping. The images used for the example given in section 4.9 are shown in Figure 11.12 & Figure 11.13.

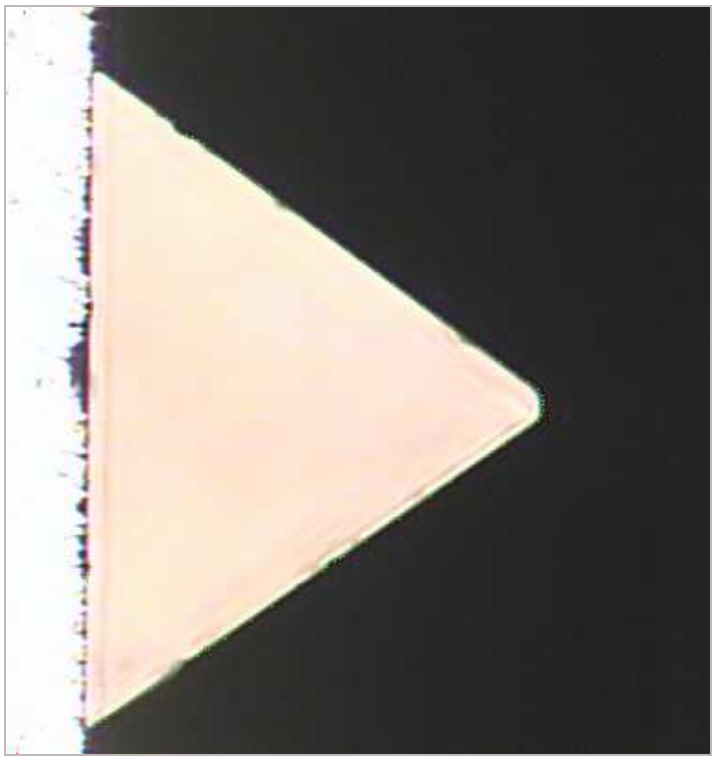

Figure 11.12 Details the layered image with the coloured points applied the trapezoidal channel.

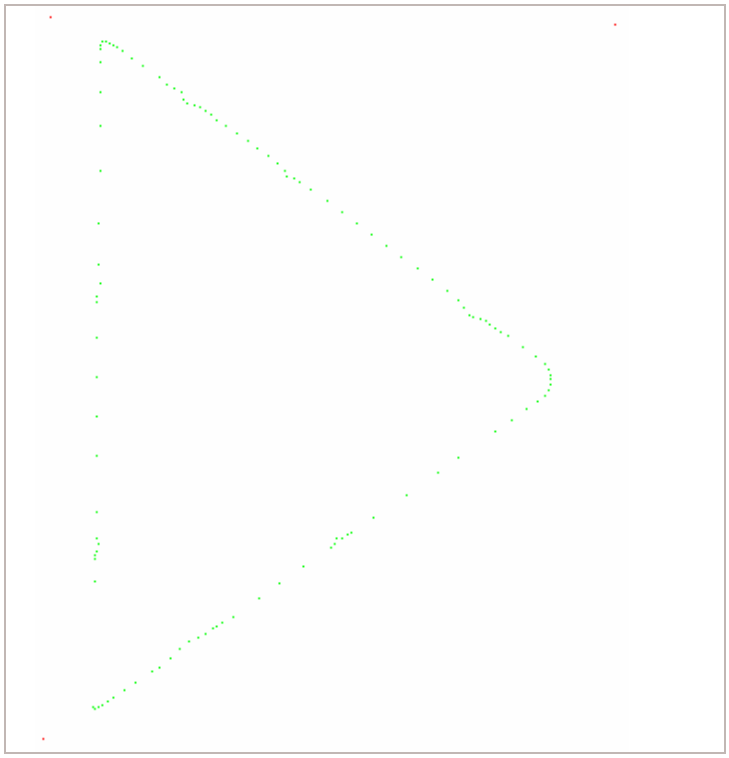

Figure 11.13 Shows the gif file scanned by the MATLAB program for section 4.9.

D. Additional Results Section

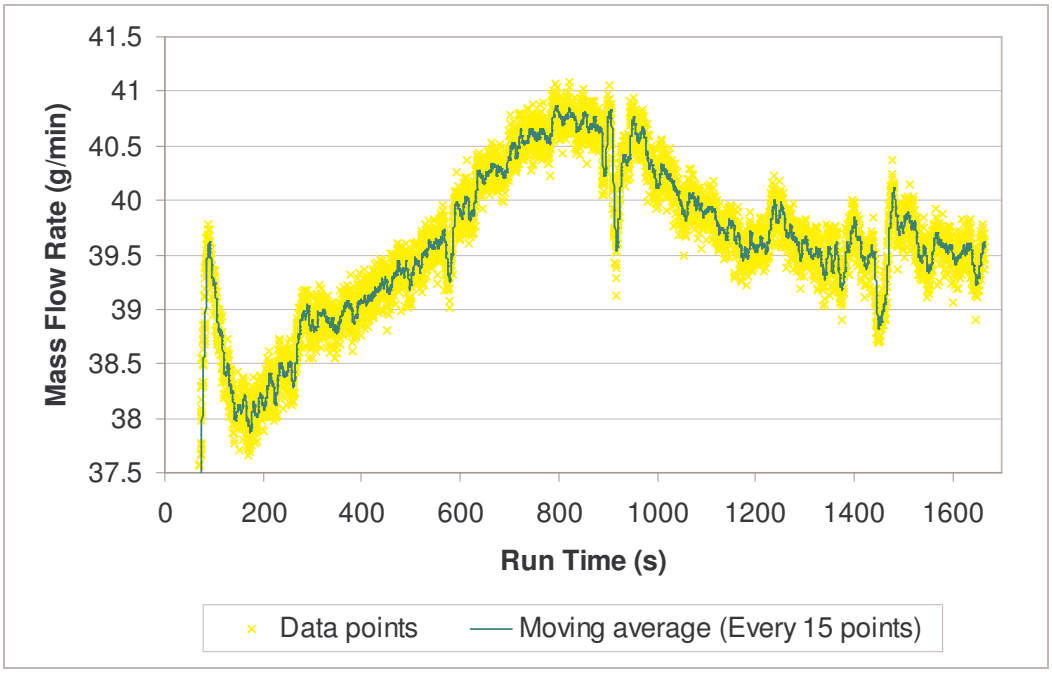

Figure 11.14 Details the variations of mass flow rate as steady state conditions are approached.

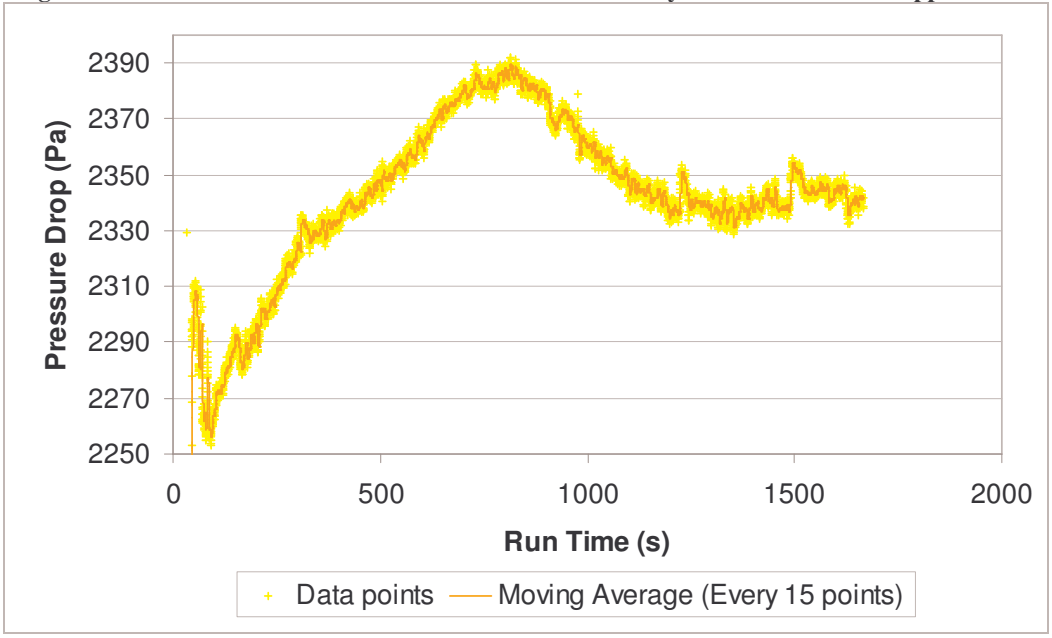

Figure 11.15 Details the variations of Pressure Drop as steady state conditions are approached.

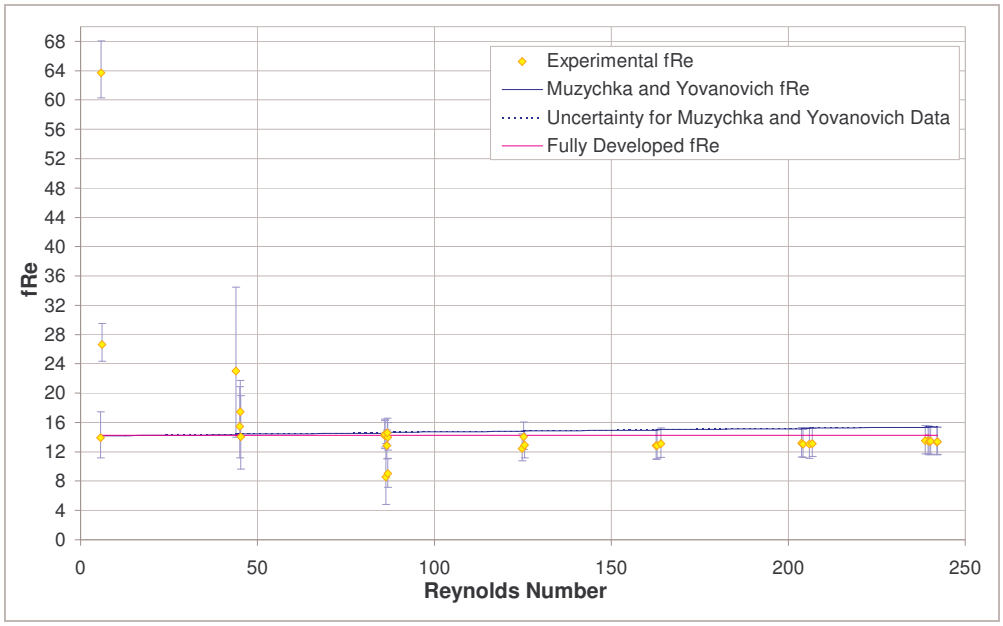

Figure 11.16 Shows the Full graph of the fRe plotted against the Re values used for the results section.